Master Thesis

titled

Optically thin clouds over Ny-Ålesund: Dependence on meteorological parameters and effect on the surface radiation budget

prepared at the

Alfred Wegener Institute
Helmholtz Centre for Polar and Marine Research
Division Physics of the Atmosphere, Potsdam

submitted to

University of Potsdam
Department of Physics and Astronomy

handed in by

Antje Kautzleben

First Referee	Prof. Dr. Klaus Dethloff
Second Referee	Prof. Dr. Frank Spahn

Potsdam, May 29, 2017

Contents

1 Zusammenfassung

Diese Arbeit befasst sich mit den Eigenschaften (optisch) dünner Wolken über Ny-Ålesund, Spitzbergen, und ihrer Strahlungswirkung am Boden. Dafür werden Daten des atmosphärischen Observatoriums der AWIPEV Station verwendet.
Den Definitionen von Sassen and Cho (1992) und Guerrero-Rascado et al. (2013) folgend werden Wolken mit einer optischen Dicke kleiner als 0.3 als optisch dünn und zwischen 0.3 und 10 als optisch dicht bezeichnet. Die optische Dicke ist definiert als das Integral über die Extinktion der Wolke in Zenitrichtung. In dieser Arbeit liegt der Fokus auf der Untersuchung von optischen Wolkeneigenschaften mit einem Photometer und Lidar, deshalb werden Wolken mit optischer Dicke kleiner als 3 untersucht.
Der Grad der Bewölkung über Ny-Ålesung wird aus Ceilometerdaten von Januar 2012 bis Dezember 2016 abgeleitet. Die Analyse ergibt eine Übereinstimmung des allgemeinen Verlaufs mit der Studie von Shupe et al. (2011), jedoch sind die Werte insgesamt größer. Die Häufigkeit der gemessenen Wolkenunterkanten gegenüber klarem Himmel ist im Sommer am größten und im Frühling am geringsten. Das Bedeckungsminimum liegt mit April einen Monat später als bei der Vergleichsstudie.
Zwei Fallstudien werden vorgestellt und folgende Fragen werden beantwortet: Wie ist die Wetterlage, wenn die Wolken auftreten? Wie verhält sich der Aerosolhintergrund? Was sind die optischen und Strahlungseigenschaften der Wolken? Wie ist ihre räumliche und zeitliche Ausdehnung? Wie gut passen die Ergebnisse der verwendeten Messgeräte zusammen? Welchen Einfluss haben die Wolken auf die Strahlungsbilanz am Boden? Ist es möglich, die Strahlungswirkung mit einem einfachen Modell zu reproduzieren?
Der Netto-Strahlungseffekt der Wolken auf den Boden ist definiert als die Differenz aus der Strahlungsbilanz am Boden mit Wolkeneinfluss minus der Strahlungsbilanz am Boden bei klarem Himmel. Es werden drei Methoden für die Bestimmung der Strahlungswirkung der Wolken vorgestellt und angewandt: für den Fall einer kleinräumigen Wolke am 6. April 2014 wird die Strahlungsbilanz des klaren Himmels abgeleitet aus Messungen der Strahlungsbilanz direkt vor und nach der Wolke mit einer linearen Interpolation für die Zeit dazwischen. Am Beispiel des 8. Mai 2015 mit Bewölkung über mehrere Stunden werden zwei Methoden verglichen: Die erste basiert auf dem Vergleich der Strahlungsmessungen mit einem klaren Vergleichstag (8. Mai 2012) unter Berücksichtigung der unterschiedlichen Aerosolbelastung und unterschiedlichen Albedo. Die zweite Methode realisiert ein einfaches Strahlungsmodell von Shupe and Intrieri (2004), womit die Strahlungsbilanz eines klaren 8. Mai 2015 und die Strahlungsbilanz der Wolke simuliert werden.
Die Fallstudie zum 6. April betrachtet kleinskalige Mischphasenwolken, die in der Lage sind, die Netto-Strahlungsbilanz am Boden um ein Drittel zu reduzieren. Eine Kombination von Messungen in Richtung Sonne, in Richtung Zenit und für den gesamten Halbraum ist schwierig auf diesen Zeit- und Raumskalen, selbst unter Berücksichtigung der Windverhältnisse. Die Extinktion der Wolken ist entgegen der Erwartung wellenlängenabhängig.

Die Fallstudie zum 8. Mai behandelt Eiswolken mit einer hohen vertikalen Ausdehnung von ca. 2 km, kleiner optischer Dicke von ca. 0.6, mit kleinem Lidarverhältnis von 16 ±4 und kleiner Volumendepolarisation von 0.03 bis 0.1. Während im Lidar KARL bereits Mehrfachstreuung die Datenauswertung erschwert, registriert das Ceilometer große Teile der Wolke nicht. Zudem liegen die gemessenen Wolkenunterkanten des Ceilometers systematisch zu hoch. Der maximale Strahlungseffekt der Wolken wurde bestimmt zu -53 W/m^2 ± 21 W/m^2. Der Strahlungseffekt ist überwiegend negativ (abkühlend). Für kurze Zeit ist der Strahlungseffekt positiv, während die ausgesandte langwellige Strahlung der Wolke den Boden erwärmt und die Wolke die direkte Sonneneinstrahlung nicht blockiert. Betrachtungen der Position der Wolken im Verhältnis zum Zenit des Beobachtungspunktes und zum Sonnenstand sind wichtig für die Beurteilung des Effektes auf die Strahlungsbilanz am Boden. Das einfache Strahlungsmodell von Shupe and Intrieri (2004) kann die gemessene Strahlungsbilanz ungefähr reproduzieren, jedoch fehlen Details, die sich aus Betrachtung der diffusen Strahlung ergeben.

2 Introduction

The Arctic is of special research interest, as it warms much faster than the global average, a phenomenon referred to as Arctic Amplification (Maturilli et al. (2015), Sedlar et al. (2010), Serreze and Barry (2011), Solomon (2007), Wendisch et al. (2017)). Clouds play an important role in Arctic climate because they influence the surface radiation budget sensitively. They play a considerable role for the beginning of snowmelt (Zhang et al. (1996)) and in formating, preserving or melting of sea-ice (Shupe and Intrieri (2004)). In the Arctic, clouds have a cooling effect only during midsummer and a warming effect for the rest of the year (Bednorz et al. (2014), Curry et al. (1996), Intrieri (2002), Shupe and Intrieri (2004)).

There are two dominant states of the Arctic atmosphere with respect to the longwave radiative budget. They were discovered in SHEBA data by Shupe and Intrieri (2004) and investigated further especially for Arctic winter time by Stramler et al. (2011) and Graham et al. (2016). One is called the "radiatively clear state" and is "characterized by cold surface temperatures, a strong surface inversion, and a large negative (upward) net longwave radiative flux (Stramler et al. (2011), Pithan et al. (2013), Raddatz et al. (2014))" (cited from Graham et al. (2016)). The second state is called "opaquely cloudy state" and has a net longwave radiative flux of around 0 $W\,m^{-2}$ and features higher surface temperature and lower surface pressure than the first state (Graham et al. (2016)). Graham et al. (2016) say that the clear state refers not only to cloud-free conditions but also includes optically thin ice-clouds. Mixed-phase clouds have a large impact on the net longwave radiative flux in all seasons (Graham et al. (2016)). The two states were also found during measurement campaigns in other regions of the Arctic: in the Canadian Arctic winter over sea-ice (Raddatz et al. (2014)), in the European Arctic during the N-ICE-campaign (Graham et al. (2016)) and satellite data also shows that these two states are found in the Arctic basin (Stramler et al. (2011), Cesana et al. (2012)). This thesis investigates the impact of optically thin clouds during times of the radiatively clear state.

This work addresses several aspects of thin cloud observations at the Arctic Research Station AWIPEV. First, typical definitions of thin clouds in the Arctic and their importance for the surface radiation balance are reviewed in chapter 3. Chapter 4 introduces the measurements conducted at AWIPEV which are suitable for the investigation of thin clouds. In addition, the methods of deriving quantities to characterize thin cloud properties and to measure their effect on the surface radiation budget are explained. The continuously running ceilometer allows to quantify cloud occurrence in the recent years. The results of the statistical analysis are presented in chapter 5. Thereafter, two particular examples of thin clouds are examined in detailed case studies in chapters 6 and 7. Research questions for these case studies are: What is the meteorological situation when the clouds in the selected examples occur? How does the aerosol background behave? What are the optical and radiative properties of the clouds and what is the time and space of their appearance? How well do the measurement results of the different instruments fit together? What

is the clouds' effect on the surface radiation budget? Is it possible to reproduce the radiative effect with a simple model? The results are summarized in chapter 8. The outlook contains suggestions for processing improvements and adjustments for future observational studies of thin clouds at Ny-Ålesund.

3 Thin clouds in the Arctic

3.1 Definition of thin clouds

There is no generally accepted definition for the term thin cloud. Authors distinguish between thin and dense/thick clouds depending on the cloud's phase composition and on the measurement instrument used in the investigation. According to a paper on thin liquid water clouds by Turner et al. (2007), liquid-bearing clouds are called thin when they have a liquid water path (LWP) of less than $100\,\mathrm{g\,m^{-2}}$. This is a comparatively large amount. According to Shupe and Intrieri (2004) around 80% of the Arctic liquid-bearing clouds have a LWP lower than $100\,\mathrm{g\,m^{-2}}$.
A distinguished categorization of high-altitude ice clouds (cirrus clouds) in the lidar community has been made by Sassen and Cho (1992). They calculate the cloud optical depth (COD) from backscatter signals from a ruby lidar. Cloud optical depth is defined as the integral over the vertical extinction profile through the cloud. The COD "is the most fundamental cloud property determining the Earth's radiative energy balance" (Chiu et al. (2010)). Sassen and Cho (1992) suggest to categorize cirrus clouds with a COD lower than 0.03 as 'subvisible' clouds, with a COD between 0.03 and 0.3 as 'thin' clouds and a COD of 0.3 up to 3 as 'opaque' cirrus. A COD of 3 was chosen as an upper limit because at this high optical thickness the emitted laser light is attenuated inside the cloud (Sassen and Cho (1992), Turner et al. (2007)).
Guerrero-Rascado et al. (2013) built upon the work by Sassen and Cho (1992) and describe a way to retrieve cloud optical depth with a sun-photometer for clouds with an optical thickness of up to 10. They categorize clouds with a COD between 0.3 and 10 as 'dense' and above 10 as 'thick'. A COD of 10 is the upper limit for dense clouds, since this is the optical depth at which the sun is no longer visible through the cloud (Bohren et al. (1995)).
In conclusion, measurements of the cloud optical depth and measurements of the liquid water path are needed to identify thin clouds.

3.2 Effects of thin clouds on the surface radiation budget

Ultraviolet, visible and infrared radiation dominate the radiative flow in the atmosphere (Boucher (2015)). Visible and UV radiation is usually referred to as shortwave radiation with the sun as the source. Infrared radiation is referred to as longwave radiation with the earth's ground as primary source and the atmosphere as secondary source.
Clouds can have two opposite effects on the surface radiation budget. Clouds may heat or cool the surface in comparison to clear sky conditions (Shupe and Intrieri (2004), Turner et al. (2007)). Clouds cool by reflecting the solar radiation back to space. Clouds warm by emitting longwave radiation (Shupe and Intrieri (2004)) and by being opaque for the upwelling longwave radiation from the ground (Turner et al. (2007)). The net effect "depends not only on cloud amount but also on cloud base height, the amount and phase of

condensed water, particle size and shape, optical depth, and ice/water contents (e.g. Curry and Ebert (1992))" (cited from Intrieri (2002)).
Turner et al. (2007) present a model sensitivity study of how a little increase in liquid water content changes the longwave and shortwave radiative budget. The study was done for standard mid-latitude summer and winter temperature and water vapor content conditions. Therefore, the values are expected to differ from Arctic conditions because of polar day or night, a much higher surface albedo, colder temperatures and a lower water vapor content. However, the shape of the flux functions over LWP should be similar. It is restricted to complete overcast conditions. According to Turner et al. (2007) net longwave fluxes at the surface increase with increasing LWP up to $20\,\mathrm{gm}^{-2}$. Then, clouds become opaque for longwave radiation. Above $40\,\mathrm{gm}^{-2}$ changes in the LWP don't increase the longwave fluxes further. The longwave radiation is then dominated by the cloud's temperature (Bennartz et al. (2013)). The downward shortwave radiation decreases with increasing LWP. There is no saturation of the decrease of shortwave radiation for a LWP below $100\,\mathrm{gm}^{-2}$ (Turner et al. (2007)).
Bennartz et al. (2013) build upon the work of Turner et al. (2007). They present a case study of the 2012 extreme melting event of the Greenland ice shield and analyze the effect of clouds with different LWPs on the ice shield's surface temperature. They come to the conclusion that clouds which are thick enough to be opaque for the upwelling infrared radiation and thin enough for the downwelling solar radiation have the highest effect on the surface radiation budget. For that specific event and location their energy balance model suggests that low-level clouds with LWP between 10 and $40\,\mathrm{gm}^{-2}$ have been the crucial part of the cause of the melting.
Cirrus clouds are an important component in the climate system (Guerrero-Rascado et al. (2013), Solomon (2007)), but "the fundamental details of the microphysical processes of ice clouds are still poorly understood" (Krämer et al. (2016)). Chen et al. (2000) find that although the effect of cirrus clouds on the surface radiation budget is small compared to low-level clouds (roughly by a factor four on average), the cumulative effect of cirrus and stratus clouds is similar due to their high occurrence fraction (Dupont and Haeffelin (2008)).

4 Instruments, data and physical quantities

This thesis makes use of data of several measurement instruments located in Ny-Ålesund, Spitsbergen in the vicinity of the AWIPEV station, formerly known as Koldewey station, at 78.9° N and 11.9° E. The station is situated at the southern coast of Kongsfjord, which is oriented in southeast-northwest direction and surrounded by mountains reaching up to 800 m. Wind below 500 m is channeled parallel to the fjord axis and blows mainly from southeast in all seasons (Burgemeister (2013), Maturilli and Kayser (2016), Schulz (2012)). Wind into the fjord in northwestern direction is less frequent (Burgemeister (2013), Maturilli and Kayser (2016)). This occurs mainly in summer and is connected to a synoptic flow from the same direction whereas the south-easterly flow can occur with different synoptic flows (Burgemeister (2013)). Climatologies from Ny-Ålesund for surface meteorology are given and discussed in Maturilli et al. (2013), climatologies for surface radiation can be found in Maturilli et al. (2015) and upper-air climatology is discussed in Maturilli and Kayser (2016).
Measurement principles, technical specifications and methods to derive physical quantities from all the instruments used in this thesis are addressed in this chapter in the following order: First, the lidar principle is explained. It is the basic principle of the active remote sensing instruments Koldewey Aerosol Raman Lidar (KARL), laser-ceilometer and wind lidar, which are explained afterwards. Next, the passive remote sensing instruments sun-photometer and microwave radiometer (MWR) are explained. Then, the in-situ radio soundings are described briefly. Lastly, Baseline Surface Radiation Network (BSRN) radiation measurements are described and a simple model for the influence of clouds on the surface radiation is presented.

4.1 Lidar principle

A lidar, short for light detection and ranging, is an active remote sensing instrument for atmospheric investigation. It consists of a pulsed laser which either emits to zenith from ground or is installed on a satellite and emits in nadir direction. Emitted light is scattered and absorbed in the atmosphere by molecules as well as by particles such as aerosols, cloud particles or precipitation. The light which is scattered back (meaning at an angle of 180°) is collected by a telescope installed either coaxially or biaxially to the emission unit. The light is then detected by a photomultiplier and recorded by a transient recorder. Since the speed of light is a fixed constant, the delay of recorded backscatter gives information about the height of the scatterers. Height resolution is calculated by $\Delta z = c/(2f)$, where c denotes the speed of light and f is the sample frequency of the transient recorder. To simplify the equations in the following section it is assumed that light which reaches the telescope was scattered only once. However, the probability for multi-scattering rises with increasing optical density in clouds. According to Chen et al. (2002) lidar signals have to be adjusted for multiple scattering effects for optical depths above 1. Since both cases studied in chapter 6 and 7 discuss clouds below this

threshold, multiple scattering is not discussed further.

4.1.1 Elastic lidar equation

The measured power P can be described by equation (1) for elastic scattering of the laser light on molecules, aerosols and hydrometeors in the atmosphere.

$$P(z,\lambda) \;=\; C(\lambda)\,\frac{O(z)}{z^2}\,\beta(z,\lambda)\,\exp\left(-2\int_0^z \alpha(z',\lambda)dz'\right) \tag{1}$$

For each wavelength λ one receives a profile of power over range $z = c/2t$. C represents the height-independent instrumental parameters. The most important amongst them is the laser power, which is dependent on λ. C changes slowly with temperature due to the temperature-dependent optical components and is therefore unknown. A possible way to determine C is the two-stream method, as was done and described in Stachlewska and Ritter (2010). $O(z)$ represents the overlap correction function, which is unity above the height where full overlap between the telescope's field of view and the image of the laser beam is reached. The overlap function increases from the ground to the overlap height from zero to unity. The correction function is determined by the manufacturer for the commercial instruments wind lidar and ceilometer. We use the ceilometer's signal to correct the signals from KARL down to an altitude as low as 600 m. The division by z^2 in equation (1) delineates from a spherical wave which is reemitted by the scattering particles in the atmosphere. The extensive quantity β represents the backscatter coefficient (unit $\mathrm{m^{-1}sr^{-1}}$). The exponential term in equation (1) describes total transmission, i.e. the integral over the extinction α (unit $\mathrm{m^{-1}}$) multiplied by two, since light propagates through air on the way from and again back to the lidar. Transmission is one close to the lidar and decreases with pollution or cloudiness of the air. The laser light interacts in the atmosphere with molecules (dominated by N_2 and O_2), which are orders of magnitude smaller than the wavelengths used by the lidar and therefore the scattering can be described with the Rayleigh theory. Aerosols have sizes either in the same magnitude as the incident radiation or larger. The scattering by aerosols is usually referred to as Mie scattering, although this theory includes Rayleigh theory as a limiting case. Mie theory assumes a spherical shape of the scattering particles. Aerosols differ from this shape but nonetheless Mie theory is sometimes a good approximation. Both β and α can be subdivided into an aerosol part and a molecular part (see eq. (2) for β, α can be expressed in the same way).

$$\beta(z,\lambda) \;=\; \beta^{aer}(z,\lambda) + \beta^{mol}(z,\lambda) \tag{2}$$

The molecular scattering and extinction can be calculated from the product of the Rayleigh cross section σ^{mol} and the number concentration of molecules N_R (eq. (3)). The number concentration is proportional to the air density, which can be calculated with the ideal gas equation and the pressure and temperature profile, which are measured with daily radiosondes launched in Ny-Ålesund.

The aerosol cross section σ^{aer} is in principle unknown. It is influenced by the shape s, diameter r and the dispersive complex refractive index m (eq. (4)). n^{aer} represents the number concentration distribution at a certain distance z from the lidar. Integrating n over shape and size yields the number of particles per volume N.

$$\beta^{mol}(z,\lambda) = \sigma^{mol}(\lambda) \cdot N_R(z) \tag{3}$$

$$\beta^{aer}(z,\lambda) = \int_0^{r_{max}} \int_{sphere}^{bar} \sigma^{aer}(m(\lambda),r,s)\, n^{aer}(z,r,s)\, \mathrm{d}s\, \mathrm{d}r \tag{4}$$

Shape, size and complex refractive index cannot be determined by just one measured power $P(z,\lambda)$. However, the received power P is an indicator for the relative number concentration of scattering particles. β and α can be retrieved from the elastic lidar equation with the so-called Klett algorithm.

4.1.2 Retrieval of backscatter and extinction with the Klett algorithm

To solve the lidar equation Klett (1981) suggested the following approach. First he defines a logarithmic range corrected signal variable $S(z)$

$$S(z) = \ln\left(P(z)\, z^2\right). \tag{5}$$

The elastic lidar equation can then be written as a differential equation

$$\frac{\mathrm{d}S}{\mathrm{d}z} = \frac{1}{\beta}\frac{\mathrm{d}\beta}{\mathrm{d}z} - 2\alpha. \tag{6}$$

Equation 6 still has two unknown variables: β and α. For a homogeneous atmosphere the slope of β is zero. This yields a direct relation between S and α:

$$\alpha_{hom} = -\frac{1}{2}\frac{\mathrm{d}S}{\mathrm{d}z}. \tag{7}$$

However this relation assumes $\beta^{-1}|\mathrm{d}\beta/\mathrm{d}z| << 2\alpha$. In a dense cloud, fog or smoke this is not the case, because of large local inhomogeneities. To solve equation 6 Klett (1985) suggested to substitute α with a parameter L times β:

$$\alpha(z) = L(z)\,\beta(z). \tag{8}$$

L is nowadays known as the lidar ratio (LR). Klett (1985) expanded the solution for particle scattering and Rayleigh scattering following the comments from Fernald (1984). This expands equation 6 to a contribution by particles (index *aer*) as Mie scatterers and a contribution from the molecular scatterers which produce Rayleigh radiation (index *mol*):

$$\alpha(z) \;=\; L^{aer}(z)\,\beta^{aer}(z) + L^{mol}\,\beta^{mol}(z). \tag{9}$$

The particle lidar ratio L^{aer} depends on the incident wavelength, particle size and shape. The Rayleigh lidar ratio L^{mol} is given as $L^{mol}(z) = (8\pi)/3$. Substituting these two into equation 6 yields:

$$\frac{\mathrm{d}S}{\mathrm{d}z} = \frac{1}{\beta}\frac{\mathrm{d}\beta}{\mathrm{d}z} - 2(L^{aer}\beta^{aer} + L^{mol}\beta^{mol}). \tag{10}$$

Using also $\beta = \beta^{aer} + \beta^{mol}$ and rearranging gives:

$$\frac{\mathrm{d}S}{\mathrm{d}z} = \frac{1}{\beta}\frac{\mathrm{d}\beta}{\mathrm{d}z} - 2L^{aer}\beta + 2(L^{aer} - L^{mol})\beta^{mol}. \tag{11}$$

Klett (1985) defined a new signal variable S' and expressed it in a system-independent form to a reference altitude z_m with $S_m = S(z_m)$:

$$S' - S'_m = S - S_m + 2L^{mol}\int_z^{z_m} \beta^{mol}\mathrm{d}z' - 2\int_z^{z_m} L^{aer}\beta^{mol}\mathrm{d}z'. \tag{12}$$

The differential equation for S' looks similar to the differential equation 6:

$$\frac{\mathrm{d}S'}{\mathrm{d}z} = \frac{1}{\beta}\frac{\mathrm{d}\beta}{\mathrm{d}z} - 2L^{aer}\beta. \tag{13}$$

This is a nonlinear ordinary differential equation of the Bernoulli form. After rearrangement with a new unknown, which is the reciprocal of β (Bernoulli substitution), the equation can be solved. The solution for the backscatter is:

$$\beta(z) = \frac{exp(S' - S'_m)}{\beta^{-1}(z_m) + 2\int_z^{z_m} L^{aer}\,exp(S' - S'_m)\mathrm{d}z'}. \tag{14}$$

The reference level z_m is set at great distance from the lidar, preferably in a clear area. There, the so-called backscatter ratio $R = \beta(z_m)/(\beta^{mol}(z_m)) = (\beta^{aer}(z_m) + \beta^{mol}(z_m))/\beta^{mol}(z_m)$ is used as a boundary condition (Ansmann et al. (1992)). Moreover, a lidar ratio is guessed for the whole profile. Choosing a correct LR is not crucial, but assuming a realistic backscatter ratio is important (Klett (1985)).

4.1.3 Retrieval of backscatter and extinction with the Ansmann method

Ansmann et al. (1992) introduced the retrieval of extinction profiles from Raman shifted backscatter. This directly gives a particle extinction. About one in thousand N_2-molecules excited with light with a wavelength of 532 nm does not

return to its ground vibrational-rotational state but to a higher vibrational-rotational state and emits at a wavelength of 607 nm as a result. This gives the inelastic lidar equation (Ansmann et al. (1992)):

$$\begin{aligned} P_{\lambda^{mol}}(z) = & C_{\lambda^{mol}} \frac{O(z)}{z^2} N_R(z) \mathrm{d}\sigma_{\lambda^{mol}}(\pi) \\ & \cdot \exp\left(-\int_0^z \alpha_{\lambda_0}^{mol}(z') + \alpha_{\lambda^{mol}}^{mol}(z') \mathrm{d}z'\right) \\ & \cdot \exp\left(-\int_0^z \alpha_{\lambda_0}^{aer}(z') + \alpha_{\lambda^{mol}}^{aer}(z') \mathrm{d}z'\right), \end{aligned} \tag{15}$$

with λ^{mol} referring to Raman and λ_0 to elastic scattering. The amount of molecular backscatter is proportional to the amount of nitrogen in the atmosphere, which follows the density of the air which can be calculated with the ideal gas equation. Measurements of temperature and pressure from daily radio soundings serve as input for that equation. Rearranging the above equation and assuming the particle extinction to be proportional to λ^{-k} yields the elastic particle extinction (Ansmann et al. (1992)):

$$\alpha_{\lambda_0}^{aer}(z) = \frac{\frac{\mathrm{d}}{\mathrm{d}z}\left(\ln \frac{N_R(z)}{P_{\lambda^{mol}}(z) z^2}\right) - \alpha_{\lambda_0}^{mol}(z) - \alpha_{\lambda^{mol}}^{mol}(z)}{1 + \left(\frac{\lambda_0}{\lambda^{mol}}\right)^k} \tag{16}$$

Dividing the elastic lidar equation by the Raman lidar equation and dividing each equation by assumed boundary conditions for $P_{\lambda_0}(z_m)$ and $P_{\lambda^{mol}}(z_m)$ gives:

$$\frac{P_{\lambda_0}(z) P_{\lambda^{mol}}(z_m)}{P_{\lambda^{mol}}(z) P_{\lambda_0}(z_m)}, \tag{17}$$

and rearranging this yields a solution for the particle backscatter (Ansmann et al. (1992)):

$$\begin{aligned} \beta_{\lambda_0}^{aer}(z) = & -\beta_{\lambda_0}^{mol}(z) + \left(\beta_{\lambda_0}^{aer}(z_m) + \beta_{\lambda_0}^{mol}(z_m)\right) \\ & \cdot \frac{P_{\lambda^{mol}}(z_m) P_{\lambda_0}(z) N_R(z)}{P_{\lambda_0}(z_m) P_{\lambda^{mol}}(z) N_R(z_m)} \\ & \cdot \frac{exp\left(-\int_{z_0}^z \alpha_{\lambda mol}^{aer}(z') + \alpha_{\lambda mol}^{mol}(z') \mathrm{d}z'\right)}{exp\left(-\int_{z_0}^z \alpha_{\lambda_0}^{aer}(z') + \alpha_{\lambda_0}^{mol}(z') \mathrm{d}z'\right)}. \end{aligned} \tag{18}$$

The reference height is the same as for the Klett algorithm. Using both Klett and Ansmann method yields two profiles each for α and β. The Ansmann method is better for signals near the lidar since the noise is low here. It also gives a lidar ratio which can be used to calibrate the Klett method. The Klett method is superior for signals far away from the lidar. Comparing and com-

bining both signals yield results closer to the actual atmospheric profiles than one method alone could produce.

4.1.4 Intensive quantities from elastic lidar equation

To get information about shape and size of the particles, a combination of two channels for each information is used. The ratio of the backscattered intensities of the perpendicularly and parallelly polarized light of equal wavelength is called volume depolarization (VD, equation (19)). It provides information about the shape of the particles. The VD of air (O_2 and N_2 molecules) is known to be 1.4 %. Thus, the VD can be calibrated at altitudes with clear sky with k_{VD} in equation (20). Spherical particles, such as water droplets, do not change the polarization of the reflected light and thus the VD is near 0 %. Pure sulfate aerosols are hydrophilic and have a VD below 1 % . Crystalline sea salt has a high depolarization at around 10 %. Spurious ice crystals depolarize at 4-6 % while in cirrus clouds depolarization can be higher than 60 %, depending on the particle micro-physics. In conclusion, water and ice in clouds can be easily distinguished with the depolarization values in the cloudy area.

$$VD = \frac{P(\lambda)_{\perp}}{P(\lambda)_{\parallel}} \cdot \frac{1}{k_{VD}} \tag{19}$$

$$k_{VD} = \frac{P(\lambda,\ \text{clear sky})_{\perp}}{P(\lambda,\ \text{clear sky})_{\parallel}} \cdot 1.4\% \tag{20}$$

The ratio of aerosol backscatter at two wavelength, e.g. 355 nm and 532 nm, is called color ratio (CR, equation (21)). CR contains information about the size of scattering particles. As explained by Mie theory, backscatter is proportional to λ^0 for bigger and to λ^{-4} for smaller sizes. λ^{-4} is the case for Rayleigh scattering, λ^0 corresponds to particles with large diameters, where scattered light has no wavelength dependency, also known as the geometric optics limit.

$$CR = \frac{\beta_{aer}(355)}{\beta_{aer}(532)} \tag{21}$$

4.2 KARL

KARL stands for Koldewey Aerosol Raman Lidar. It uses a ND:YAG laser and emits at 1064 nm with circular polarized light and at 532 nm (frequency-doubled) and 355 nm (frequency-trippled) with linearly polarized light. The backscattered light at 532 nm and 355 nm is subdivided in the receiving optics into parallel and perpendicular polarized light relative to the outgoing beams. The Raman-shifted light from 532 nm is measured at 607 nm (N_2) and 660 nm (H_2O) and for 355 nm at 387 nm (H_2O) and 407 nm (H2O). Further technical details can be found in the PhD thesis by Hoffmann (2010). Raw time resolution is about 90 s. While processing, the data is reduced to yield one averaged profile about every 10 minutes.

4.3 Ceilometer

A laser ceilometer is an unpolarized one-wavelength backscatter lidar to determine cloud base height (CBH) and vertical visibility (VV). The CL51 ceilometer from Vaisala is in operation at Ny-Ålesund since September 2011. Earlier on, a LD40 ceilometer from Vaisala was in use, but products of the new CL51 look more promising, which is why only data from the new one is used. The CL51 uses an InGaAs diode laser, which emits short pulses at 910 nm. It is a class 1M laser, which means that the intensity of the ambient light is larger than the backscattered signal and therefore the laser is eye-safe. It emits a large number of pulses and the backscatter is integrated over time. Thus, random ambient noise is canceled out. The height resolution is 10 m. The ceilometer reports the CBH every 15 s in a standard LD-40 telegram. It contains information about up to three separate CBHs and the VV. The handbook defines VV as follows: VV is the altitude where the optical depth, defined as integral over extinction from the ground $OD = \int_0^{VV} \alpha(\hat{z})\mathrm{d}\hat{z}$, exceeds a certain threshold. The threshold was determined experimentally by comparing the VV determined by the human eye with results from the ceilometer and adjusting such that both report similar heights. The handbook does not explain how cloud hits are defined. It only says that the process is variable in time and space. From experience with KARL backscatter it is assumed that there is a $\mathrm{d}\beta/\mathrm{d}z$ threshold in combination with an absolute β-threshold to determine cloud affected bins since clouds can clearly be identified in KARL backscatter data by visual examination. In an iterative process cloud-affected bins are clustered to clouds and their base heights are determined. Accuracy of the CBH is considered to be around 30 m (Clothiaux et al. (2000)). Height range is 13 km. In this work only the lowermost reported cloud layer is used since this is the one with the most impact on the surface radiation. In mixed-phase clouds with a geometrically thin liquid layer on top of a geometrically thick ice layer the ceilometer reports the liquid layer as cloud base (Shupe et al. (2008)). This is probably due to low particle concentration in the ice-layer which does not produce enough backscatter.

4.4 Wind Lidar

A wind lidar measures the horizontal wind speed components U and V, vertical wind speed W and wind direction Wdir. The model "Windcube 200" by the manufacturer Leosphere continuously measures in Ny-Ålesund since December 5th 2012. It's performance was characterized in the master's thesis by Burgemeister (2013). She describes the measurement principle as follows:
Wind lidars use the Doppler effect: the wavelength of scattered light changes with wind speed along the scattering axis $\Delta\lambda/\lambda = v/c$. However, the change in wavelength is too small to be measured directly. Therefore, the outgoing laser beam is split into two parts. One part, send into the atmosphere, is scattered on aerosol particles and Doppler-shifted and then collected by a telescope. The other part is reflected back and forth inside the instrument and retains its original wavelength. The interference of both beams yields a beat with a frequency of about $3 \cdot 10^5$ Hz. The Doppler-shift and hence the wind speed

along the outgoing laser beam can be derived from this frequency. The outgoing laser beam is not pointed in zenith direction, but tilted by 15 degrees off zenith. At this solid angle the beam describes a circle around zenith. On this circle it measures four times with even distance (e.g. to north, east, south, west). The wind vector is derived from a combination of these four measurements.
Burgemeister (2013) gives these technical specifications: The laser is pulsed and has a wavelength of 1,54μm. This makes the instrument eye-safe and therefore it can be operated day and year round. This wavelength is too large for Rayleigh scattering on molecules and therefore aerosols as so-called tracers are needed as scattering particles. The altitude range is in theory 100 m up to 5 km, but the detection range is limited to the availability of tracers and, therefore, reduced to altitudes typically up to 1-1.5 km in the clear Arctic atmosphere. The height resolution is 50 m. The integration time for each measurement set is 10 s. In a final step, all variables are averaged over ten minutes to increase the signal-to-noise ratio.

4.5 Sun-photometer

A sun-photometer measures the intensity of direct solar radiation reaching the ground at distinct wavelengths, which is transformed into voltage signals. With a gauge function (obtained through Langley-Calibration) and calculation of the amount of light arriving at top-of-the-atmosphere (TOA), these voltages can be transformed into an aerosol optical depth (AOD). The following subsections cover the measurement principle, the definition of AOD, COD and Ångström exponent (AE), and the retrieval of AOD and AE and lastly the retrieval of COD.

4.5.1 Measurement principle

Stock (2010) described the general measurement principle as follows: A sun-photometer uses a tracking unit directing the photometer to the sun. The instrument has a small field-of-view (1°) to include only direct solar radiation. A lens focuses the collected light on an interference filter, which reduces the incoming broad spectrum to a narrow wavelength band with a full width half maximum of 3-10 nm. After an aperture stop, a photo diode transforms the incoming intensity to an electric signal. The SP1A currently used in Ny-Ålesund has a filter bank with ten different interference filters between 369 and 1022 nm.

4.5.2 Aerosol Optical Depth and Ångström exponent

The optical depth (OD) τ is defined in the Bouguer-Lambert-Beer law (e.g. Guerrero-Rascado et al. (2013)):

$$I = I_0 \, \mathrm{e}^{-m\,\tau}, \tag{22}$$

$$\tau = \tau_r + \tau_g + \tau_a + \tau_c. \tag{23}$$

I is the intensity of the light beam that reaches the surface, I_0 is the intensity of light at the top-of-the-atmosphere. The optical thickness τ represents the amount of light that is extinguished when the light passes through the air mass m, which can be approximated with the solar zenith angle θ: $m = \frac{1}{\cos\theta}$, assuming a plane parallel atmosphere. τ_r stands for the light extinguished by Rayleigh scattering (molecular scattering), τ_o for gaseous absorption by ozone, τ_a denotes the aerosol optical depth and τ_c is the cloud optical depth. Each optical depth τ_x is the integral over the extinction coefficient (unit m^{-1}). The particle extinction is the sum of absorption and scattering (Boucher (2015)):

$$\sigma^{sca} = \int_0^\infty \pi\, r^2\, Q^{sca}(r)\, n(r)\, \mathrm{d}r, \tag{24}$$

$$\sigma^{abs} = \int_0^\infty \pi\, r^2\, Q^{abs}(r)\, n(r)\, \mathrm{d}r, \tag{25}$$

$$\tau_x = \int_0^{TOA} \sigma^{sca}(z) + \sigma^{abs}(z)\, \mathrm{d}z. \tag{26}$$

Here, r denotes the size and n(r) the particle size distribution, Q^{sca} the scattering efficiency and Q^{abs} the absorption efficiency which are both also dependent on the refractive index of the scattering particles and on the wavelength of the incident electromagnetic radiation. The spectral dependency of the AOD is measured with the Ångström exponent (AE) (Boucher (2015)):

$$AE = -\frac{ln(\tau(\lambda_2)/\tau(\lambda_2))}{ln(\lambda_1/\lambda_2)}. \tag{27}$$

The AE is an indicator for the size of the scatterers. It is worth noting, that photometer and lidar only measure a volume AE, which describes the spectral dependency of a volume of aerosols with a size distribution. AE is a good indicator for the dominating size of particles within the volume. AE values between 0 and 1 indicates large particles with diameter greater than 1μm (Stock (2010)). For AE greater than 1, aerosols with diameter between 0.2 and 0.5 μm dominate (Stock (2010)). Tomasi et al. (2007) investigated longterm Artic aerosol properties and found for background Arctic aerosol a mean AOD of 0.015 at 500 nm with AE of 1.40. Dense Arctic aerosol has a mean AOD(500 nm) of 0.08 and AE of 1, Arctic haze has a higher AOD(500 nm) of 0.15 with AE of 1.25. Clouds typically have low AE near zero (Tomasi et al. (2007)). The optical depth and AE of clouds change rapidly on a minutely timescale. Due the remote location of Ny-Ålesund and aerosol is usually already aged and fast chemical reactions already took place. Therefore, the optical properties of aerosols in the measured volume change in the course of hours.

4.5.3 AOD and AE retrieval

The AOD is determined at cloud-free conditions, i.e. when the COD is zero. The cloud screening process is described in the next subsection. The calculation

of AOD (or τ_a) is done with programs developed by Maria Stock and Holger Deckelmann (Stock (2010)). Equations (22) and (23) yield equation (28) with the specific air masses m to the respective τ and with $\tau_c = 0$:

$$\tau_a = \frac{ln\left(\frac{I_0}{I}\right) - m_r\,\tau_r - m_g\,\tau_g}{m_a}. \tag{28}$$

Stock (2010) used WMO standards (WMO (1996)) to retrieve AOD from the sun-photometer:

$$\tau_a(\lambda) = ln\frac{U_0(\lambda)}{U(\lambda)\,K\,m_a} - \frac{\tau_r(\lambda)\,m_r + \tau_o(\lambda)\,m_o}{m_a}. \tag{29}$$

U_0 represents the extraterrestrial voltage determined through the Langley calibration, U is the measured voltage, K is a factor to correct for the distance between the sun and the earth. Stock (2010) estimated the maximum error of τ_a to be ± 0.01 for $\lambda >$400 nm and ± 0.02 for $\lambda <$400 nm.
The approximation functions for τ and m used in the algorithm are listed here following the description by Stock (2010).
Rayleigh optical depth τ_r is calculated with a formula by Fröhlich and Shaw (1980) with the surface pressure p as input variable:

$$\tau_r = \frac{p}{1013.25hPa} 0.00865\lambda^{-(3.9164+0.074\lambda+\frac{0.05}{\lambda})}. \tag{30}$$

The optical depth of ozone is calculated with a formula by H.U. Dütsch (Stock (2010)):

$$\tau_o = \frac{O_{3,Dobson} O_{3,gauge}}{1000}. \tag{31}$$

The daily ozone column concentration $O_{3,Dobson}$ is measured by the Total Ozone Mapping Spectrometer from a satellite by NASA. The wavelength dependent instrumental gauge factors $O_{3,gauge}$ are determined by the manufacturer.
The relative aerosol air mass is calculated using a formula by Kasten and Young (1989):

$$m_a = \frac{1}{\sin h_s un + 0.0548(h_s un + 2.65)^{-1.452}}. \tag{32}$$

h_{sun} denotes the apparent solar elevation, which is higher than the geometrical solar elevation above the horizon. The density of air increases from the top of the atmosphere to the surface and therefore, the light is refracted. To calculate the exact apparent solar elevation we would have to know the temperature and pressure along the light path. Because this is unknown, an approximation with an ephemeris program in the style of Kaplan et al. (1989) was implemented.

The relative Rayleigh air mass is calculated with a formula by Kasten (1965):

$$m_r = \frac{1}{\sin h_sun + 0.50572(h_sun + 6.07995)^{-1.6364}}. \quad (33)$$

The relative ozone air mass is calculated with a formula by Komhyr (1980):

$$m_o = \frac{r + z_o}{\sqrt{(r + z_o)^2 - (r_E + z_s)^2 \cos {h_{sun}}^2}}. \quad (34)$$

z_o =22 km is the height of the ozone layer, z_o =10 m is the station height and r_E =6370 km is the earth's radius.
The Ångström exponent (AE) can be determined from τ_a and the corresponding wavelengths through linear regression from this relation:

$$\tau_a(\lambda) = C\,\lambda^{-AE}, \quad (35)$$
$$\ln \tau_a(\lambda) = \ln C - AE \ln \lambda. \quad (36)$$

C is the so-called turbidity parameter, the Ångström exponent is the slope of the regression line.
The air mass approximation only yields good results for solar elevation angles above 5° (Stock (2010)). Therefore, data below 5° is excluded from the analysis.

4.5.4 Cloud screening and COD retrieval

Cloud contaminated measurements of the AOD can easily be identified since scattering in clouds is less wavelength-dependent and therefore the AE is below unity. Also the COD varies from minute to minute while AOD varies on time scale of hours. The case studies in chapters 6 and 7 illustrate this.
The measured OD cannot be used when thick clouds or mountains block the direct solar radiation. Thick clouds have different scattering properties from aerosols and the above described retrieval algorithm of optical depth is not suited for this. A threshold for identifying usable data was found by visual inspection: When direct shortwave radiation is at least 120 Wm^{-2} the values of OD look reasonable. Cases with cloud-free sky before and after a cloud are utilized to extrapolate the AOD. The COD equals the measured OD at times with cloud influence minus the extrapolated AOD background. This is justified for a few hours, when AOD does not change significantly. This method reduces the number of usable cases drastically and only broken clouds can be investigated.

4.6 Microwave Radiometer

Since 2012 the AWIPEV observatory uses a Humidity And Temperature PROfiler (HATPRO) manufactured by the Radiometer Physics GmbH. It is a passive ground-based remote sensing instrument that makes use of the frequency

dependent extinction of radiation by atmospheric water vapor, oxygen and liquid clouds in the microwave range and is therefore called a microwave radiometer (MWR). Liquid clouds are semi-permeable in this range. The MWR is not sensitive to ice clouds. An additional broadband infrared radiometer measures the cloud base temperature at wavelengths between 9.2 and 10.6μm. Including this in the retrieval improves the accuracy of the humidity profiling and gives a rough estimate of the liquid water content (LWC) (Rad (2013)). Environmental temperature, pressure and humidity sensors are used to estimate the mean atmospheric temperature and the boiling temperature of nitrogen for absolute calibration. A rain sensor gives additional information for the retrieval and controls the speed of the integrated dew blower to keep the window free of ice. A GPS sensor gives the Coordinated Universal Time (UTC) for temporal synchronization. In the upcoming two subsections the LWP and integrated water vapor (IWV) are defined and the retrieval of temperature, humidity and LWP and IWV is explained.

4.6.1 Liquid water path and cloud optical depth

Liquid bearing clouds contain droplets of water with different sizes, which is physically described by the drop size distribution $n(r)$ - the number of drops per unit volume as a function of drop radius r (Turner et al. (2007)). The LWC is the integral over the mass of the drop size distribution, see equation (37) (Turner et al. (2007)). ρ_l denotes the density of liquid water. The liquid water path (LWP) equals the liquid water content integrated through the atmosphere (Turner et al. (2007)).

$$LWC = \frac{4\pi}{3}\rho_l \int r^3 n(r)\,\mathrm{d}r \tag{37}$$

$$LWP = \int_a^b LWC(z)\,\mathrm{d}z \tag{38}$$

For visible and near-infrared wavelengths, which are much smaller than droplet radius, the COD can be approximated from LWP, density and effective radius r_e, see equations (39 - 40) (Stephens (1994), Turner et al. (2007)).

$$\tau_c \approx \frac{3\,\mathrm{LWP}}{2\,\rho_l\,r_e} \tag{39}$$

$$r_e = \frac{\int_0^\infty r^3 n(r)\,\mathrm{d}r}{\int_0^\infty r^2 n(r)\,\mathrm{d}r} \tag{40}$$

The cloud optical depth τ_c is "the physical depth of the cloud measured in units of total mean-free path (Bohren and Clothiaux (2006))" (Turner et al. (2007)).

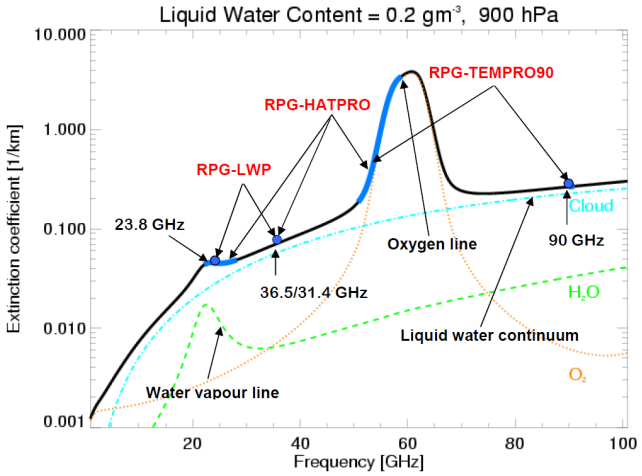

Figure 1: Extinction of microwave radiation by atmospheric water vapor, oxygen and liquid water. *Figure taken from Rad (2011)*

4.6.2 Retrieval of temperature and humidity

Atmospheric temperature profiles are derived with measurements of brightness temperatures TB at seven frequencies in the V band between 51 and 58 GHz. The atmosphere is optically thick in the center of the oxygen emission line. The atmosphere is more transparent for frequencies away from the center. Therefore, the height of origin of the measured radiation is close to the instrument for 58GHz and increases for lower frequencies (Rad (2011)).
Information on the height distribution of atmospheric water vapor is derived from seven frequencies in the K band between 22 GHz and 28 GHz, where the water vapor line is broadened by pressure by about 3 MHz/hPa between approximately 300 and 100 hPa (Rad (2011)).
LWP is usually derived from downwelling radiation at 23.8 and 31.4 GHz (Rad (2011), Marke et al. (2016)). The former is on a wing of the water vapor absorption line (see figure 1) and, therefore, influenced by water vapor as well as liquid-bearing clouds while the latter is in a region without a maximum of absorption by water vapor or oxygen.
The retrieval of the physical quantities from the measured brightness temperatures is explained in Rad (2011) as follows: An artificial neural network (ANN) is used to retrieve the output variables (profiles of temperature and humidity as well as liquid water path and integrated water vapor (IWV)). Five years of daily radio soundings were utilized to construct the ANN. The brightness temperatures TB are calculated from each radio sounding with a radiative transfer model. These simulated brightness temperatures form an input-layer for the ANN. Additional inputs are surface temperature, pressure and relative humidity plus cloud base temperature from the IR measurement. A hidden layer, consisting of a certain number of neurons, connects the simulated TB with the output variables. The data set of simulated TB and associated states of the atmosphere was subdivided into three sets to train, generalize and test the ANN.
The retrieval error is considered to be at least 20-30 g/m^2 because of the mea-

surement accuracy, uncertainties in the absorption model and in the applied retrieval method (Crewell and Löhnert (2003), Marke et al. (2016), Turner et al. (2007)).

4.7 Radiosondes

Radiosondes are compact in-situ instruments which are launched with a weather balloon into the atmosphere. The balloon is filled with helium and ascends with on average 5 m/s until it bursts because of low ambient pressure (usually at about 30 km altitude). Radiosondes provide in-situ profiles of pressure, temperature and humidity (measured with built-in sensors) as well as wind speed and direction which are derived from GPS location. Radiosondes are launched daily in Ny-Ålesund since November 1992. Since then, there have been several changes in the instrumentation. Maturilli and Kayser (2016) made an effort to homogenize this long radiosonde record and discuss trends in the upper-air meteorology. Since May 20th 2006 the RS92-SGP radiosondes from Vaisala are launched at least daily at 11 UTC (referred to as 12 UTC sondes). The data processing is done with a standard procedure developed by the GRUAN network, which provides reference-quality data (Bodeker et al. (2016), Maturilli and Kayser (2016)). During the ascent the measurement data is send to the ground receiver every second, which results in a high height resolution of 5 m on average. Further technical specifications can be found in the referenced data sheet.

4.8 BSRN

BSRN stands for Baseline Surface Radiation Network. The BSRN station in Ny-Ålesund is in operation since August 1992 with measurements of up- and downwelling long- and shortwave surface radiation (Maturilli et al. (2015)). Since August 1993 standard surface meteorology (temperature, pressure, relative humidity, wind speed and wind direction at 2 m above ground) is also in operation. The currently used instruments are: Broadband downwelling diffuse and global shortwave radiation is measured with a CMP22 Pyranometer between 200 nm and 3600 nm by Kipp & Zonen. Broadband direct shortwave radiation is measured with a CHP1 Pyrheliometer at 200-4000 nm by Kipp & Zonen. Broadband up- and downwelling longwave radiation is measured with a Precision Infrared Radiometer by Eppley Lab at 4.5-42 μm. For this thesis data from the BSRN is used to characterize the weather situation for the case studies and to evaluate the effect of the clouds on the surface radiation budget. The method for deriving the surface radiation budget and cloud radiative forcing is described in the following.

4.8.1 Surface Radiation Budget and Cloud Radiative Forcing

The net surface radiation budget (SRB) is defined in equations (41) - (43) (e.g. Maturilli et al. (2015)). SW_{down} (LW_{down}) denotes the downwelling shortwave (longwave) radiation and SW_{up} (LW_{up}) denotes the upwelling shortwave

(longwave) radiation. Downwards fluxes are defined as positive, i.e. a positive net flux is warming the surface.

$$LW_{net} = LW_{down} - LW_{up} \quad (41)$$
$$SW_{net} = SW_{down} - SW_{up} \quad (42)$$
$$SRB = LW_{net} + SW_{net} \quad (43)$$

The cloud radiative forcing (CRF) is defined by Shupe and Intrieri (2004) as "the radiative impact that clouds have on the atmosphere, surface or TOA relative to clear skies". In this study CRF refers to the effect of clouds on the surface as defined in equations (44) - (46) (adapted from Shupe and Intrieri (2004)).

$$CRF_{LW} = LW_{net}(CF) - LW_{net}(CF = 0) \quad (44)$$
$$CRF_{SW} = SW_{net}(CF) - SW_{net}(CF = 0) \quad (45)$$
$$CRF = CRF_{LW} + CRF_{SW} \quad (46)$$

CF denotes the cloud fraction, with $CF = 0$ referring to clear sky and $CF = 1$ to an overcast sky. Analogous to the net surface radiation budget a positive cloud radiative forcing corresponds to a warming effect by the clouds on the surface.

4.8.2 A simple model for cloud radiative forcing

Shupe and Intrieri (2004) use a first-order atmospheric radiative flux model to identify the atmospheric properties that shape the cloud radiative forcing. For this they make the following assumptions:
(a) The temperature profile with height $T(z)$ is not affected by clouds:
$T_{CF=1}(z) = T_{CF=0}(z)$.
(b) Clouds do not change the upwelling longwave radiation:
$LW_{up}(CF = 1) - LW_{up}(CF = 0) = 0$. LW_{up} is determined by the surface temperature.
(c) The cloud absorbs most of the downwelling longwave flux above the cloud, which comes from atmospheric aerosols and gases.
For this simple model the atmosphere is separated into three parts: above the cloud (ac), the cloud layer(c) and below the cloud (bc). An effective temperature T, broadband transmittance t and broadband emissivity ϵ are assigned to each layer. Equation (47) shows the resulting clear sky downward longwave radiation as given in Shupe and Intrieri (2004). σ is the Stefan-Boltzmann constant.

$$LW_{down}(CF = 0) = t_{bc}\sigma T_{ac}^4 + \sigma T_{bc}^4 \quad (47)$$
$$LW_{down}(CF = 1) = t_{bc}(1 - \epsilon_c)\sigma T_{ac}^4 + t_{bc}\epsilon_c\sigma T_c^4 + \sigma T_{bc}^4 + Re \quad (48)$$
$$CRF_{LW} \approx t_{bc}\epsilon_c\sigma(T_c^4 - T_{ac}^4) \quad (49)$$

Equation (48) gives the cloudy sky downward longwave radiation (adapted from Shupe and Intrieri (2004)). The term Re stands for the reflected longwave radiation by the cloud. This term can be neglected because the infrared reflectance is small compared to the cloud's emission (Shupe and Intrieri (2004), Smith et al. (1993)). Equation (48) minus (47) yields the longwave cloud radiative forcing in equation (49). The cloud's emissivity is related to the cloud longwave optical absorption depth by $\epsilon_c = 1 - e^{\tau_{clw}}$, which is dependent on microphysical properties (Shupe and Intrieri (2004)). The effective temperature above the cloud layer T_{ac} can be derived approximately from the cloud altitude and cloud effective temperature. Because the concentration of water vapor decreases exponentially with height, the temperature difference $\Delta T = T_c - T_{ac}$ increases approximately linearly with height: $\Delta T = 2.8 z_c + 20$, based on Arctic standard profiles for temperature, humidity and LW_{down} and with z_c being the cloud height in km (Shupe and Intrieri (2004)).
The net shortwave flux at the surface during clear sky can be approximated by equation (50) and during cloudy sky by equation (51).

$$SW_{net}(CF = 0) = t_{aSW} S \cos\theta \, (1 - \alpha_s) \tag{50}$$

$$SW_{net}(CF) = t_{aSW} S \cos\theta \, (1 - \alpha_s) t_{cSW} \tag{51}$$

t_{aSW} denotes the broadband atmospheric shortwave transmittance, t_{cSW} the broadband cloud shortwave transmittance, S the solar constant, α_s the surface albedo and θ the solar zenith angle.
Both components combined yield the net cloud radiative forcing in equation (52):

$$CRF \approx t_{bc} \, \epsilon_c \, \sigma \, (T_c^4 - T_{ac}^4) + t_{aSW} \, S \cos\theta \, (1 - \alpha_s) \, (t_{cSW} - 1). \tag{52}$$

Therefore, the cloud radiative forcing is mainly influenced by the transmittance below and above the cloud (aerosols, gases), the longwave emissivity and shortwave transmittance of the cloud (which depend on the microphysical composition), cloud temperature and height, the solar zenith angle and the surface albedo.

5 Cloud base statistics from Ceilometer

Data from the CL51 ceilometer in Ny-Ålesund is available for the recent five years. The main product of the ceilometer is the cloud base height (CBH). The occurrence fraction of clouds and it's dependence on season and altitude derived from the CBH is presented in the following. Meanwhile reading this analysis one should keep in mind, that the ceilometer only gives information on clouds in the zenith field of view of the instrument.

The cloud occurrence fraction (COF) is defined for this study as the number of measurements with a detected cloud base divided by the total number of measurements. The upper panel in figure 2 shows five annual cycles of monthly cloud occurrence fraction from January 2012 until December 2016 and the mean annual cycle. The lower panel shows the annual course of the mean anomaly of the monthly COF as a measure of interannual variability. April is the month with the lowest mean cloud occurrence fraction (COF) with 58% and the lowest mean anomaly with 1.9%. In May the COF jumps up to 78% . This is probably due to the onset of snow melt (or and sea-ice melt) which provides more moisture for the Arctic atmosphere. The highest mean COF measured reached 83% in September. The highest interannual variability is observed in October with a mean anomaly of 10.4%. Annual means range from 68% to 75% with longterm mean of 73%.

Figure 3 consists of boxplots of the lowest detected CBH for all months between 2012 and 2016. The monthly median (red line) cloud base heights are always lower than the mean CBHs (black rhombi), because of a higher probability for low clouds. The figure illustrates how in early summer CBHs are the lowest with a spread of the data of 95% below 4.2 km in May and June. The mean CBH is below 2 km year round. Figure 4 shows the five datasets of mean detected CBH as annual courses (colored lines) as well as the mean of all annual courses (black line). Annual means are given on the right hand side of the figure. Highest CBHs are measured in February and March with means of approx. 1.9 km and medians of approx. 1.2 km. The annual mean CBH ranges between 1.5 km and 1.8 km with a total mean of 1.6 km.

Figure 5 shows the distribution of lowest detected cloud base with height for each month of the year for the lower 2 km above ground. Each month's statistics contain cloud base heights of the respective month from all of 2012 to 2016. Shown are the results of histograms with bin widths of 100 m. The number of occurrences per bin are normalized with the number of valid measurements per month. Measurements without cloud base but with reduced range (due to precipitation or ground-based fog) are considered as invalid. The colors range from blue in winter to red in summer and back. The highest cloud fractions altitudewise are found below 1 km for all months. The maximum of occurrence is lowest in summer (650 m for July) and highest in winter (850 m for December).

Shupe et al. (2011) show an annual cycle of the monthly mean COF for Ny-Ålesund and other Arctic measurement sites (see fig. 2 in Shupe et al. (2011)). Instruments give a value of the cloud fraction for a duration of 6 hours, which is then averaged over one month. For Ny-Ålesund data from the micropulse

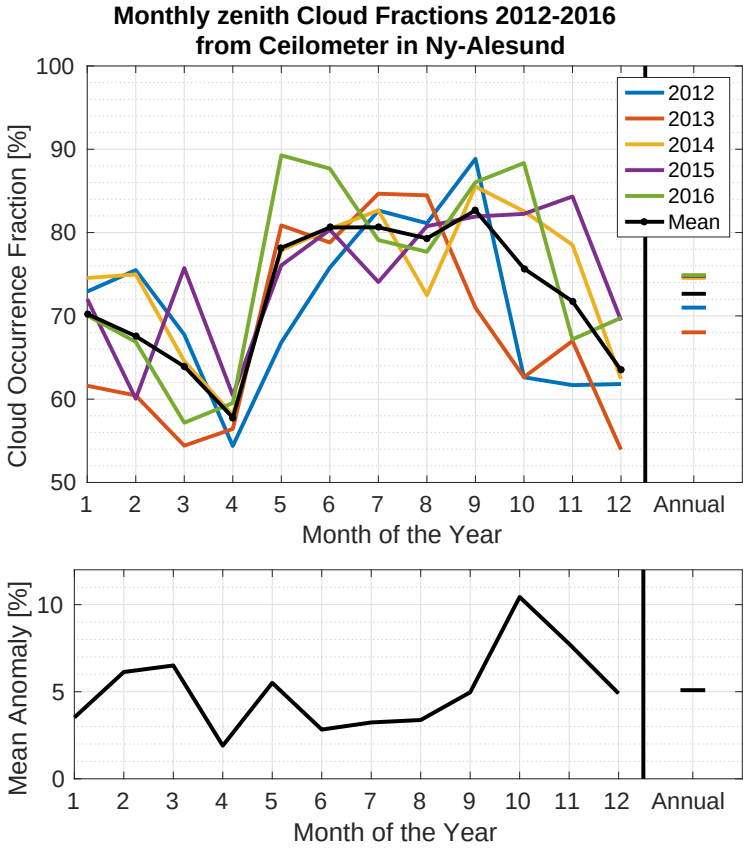

Figure 2: Upper panel: Five annual cycles of the monthly cloud occurrence fraction (COF) from January 2012 until December 2016 and the mean annual cycle are shown. The annual mean is given on the right. Lower panel: Annual course of the mean anomaly of the monthly COF and its annual mean are given. Anomaly is defined as in Shupe et al. (2011) as the absolute difference between any given monthly COF and the mean COF of the respective month, e.g. $\|COF(Jan.2014) - mean(COF(January))\|$.

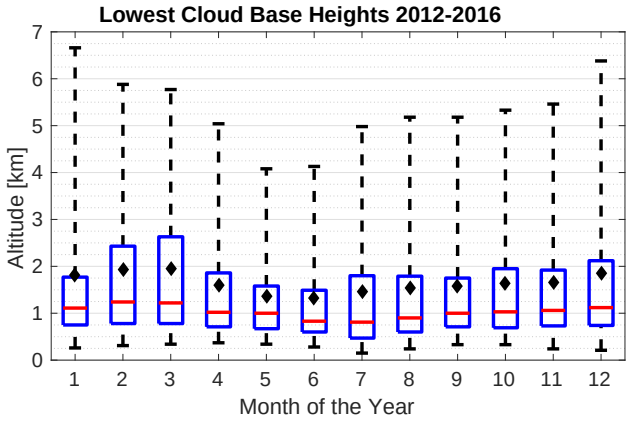

Figure 3: Boxplots of cloud base heights for each month of the year are shown. Each boxplot contains data of the respective month for the years 2012 to 2016. The red horizontal lines indicate the median of the respective dataset. The black diamonds denote the respective mean. The box's lower edge shows the 25th percentile, the upper edge the 75th percentile. The whiskers (dashed lines) point to the 5% and the 95% percentile.

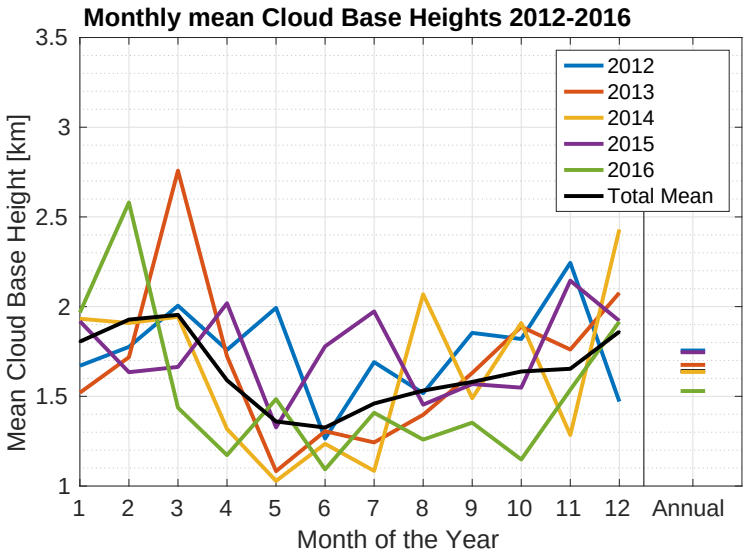

Figure 4: Five annual courses of mean cloud base height (CBH) from the years 2012 to 2016 (colored lines) and the mean annual course (black line) are shown. Annual means are given on the right.

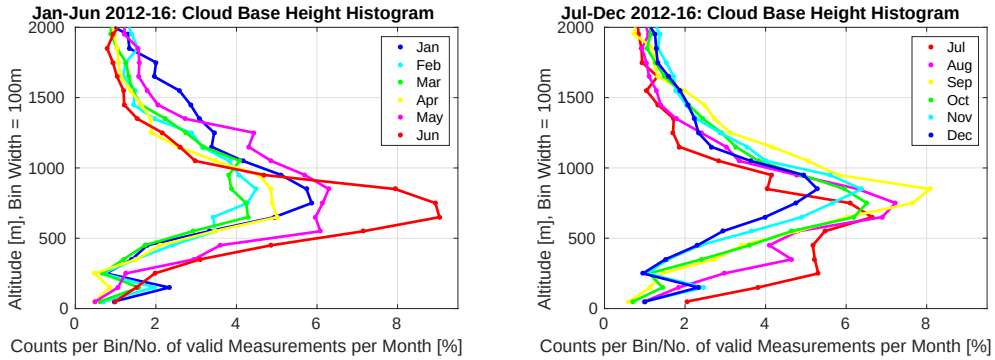

Figure 5: Histograms of cloud base heights were calculated from monthly datasets from January 2012 to December 2016. The bin width of the histograms is 100 m. The x-axes show the number of occurrences per bin normalized by the total number of valid measurements per dataset.

lidar is used, which is owned and maintained by NIPR, Japan, and hosted in the AWIPEV atmospheric observatory. It is part of the MPLNET, which provides the standardized data processing. Shupe et al. (2011) used data from March 2002 until May 2009. March was found to have the lowest mean COF with approx. 49% and August the highest one with approx. 73% . The total mean COF is 61% . Said study shows the interannual variability of the monthly COF. For their dataset, the largest intermonthly variability is in April with approx. 15% mean anomaly. The total mean anomaly of all months is approx. 8%, much higher than the mean anomaly in Barrow, Eureka and Atqasuk where it is lower than 3%.
In conclusion, the cloud fractions by Shupe et al. (2011) are lower compared to the findings in this study. The difference could be due to the different measurement period or due to the use of different instrument and methodology.

6 Case study: 6th of April 2014

Measurement results from the atmospheric observatory at AWIPEV station in Ny-Ålesund on April 6th, 2014 are presented in this chapter. First, the general weather situation is described. Then, the aerosol load on this day is characterized and subsequently properties of the clouds measured on this day are presented. Particularly, small extent, thin clouds in the afternoon are investigated in detail. Following up, a simple method to derive the cloud radiative forcing (CRF) is applied. Finally, the findings are summed up.

6.1 Weather situation

Figure 6 shows surface (2 m) pressure, temperature, humidity, wind direction and wind speed as well as the lowest CBH from the ceilometer and upwelling and downwelling longwave radiation for April 4th to 8th 2014, all measured at the AWIPEV observatory in Ny-Ålesund .

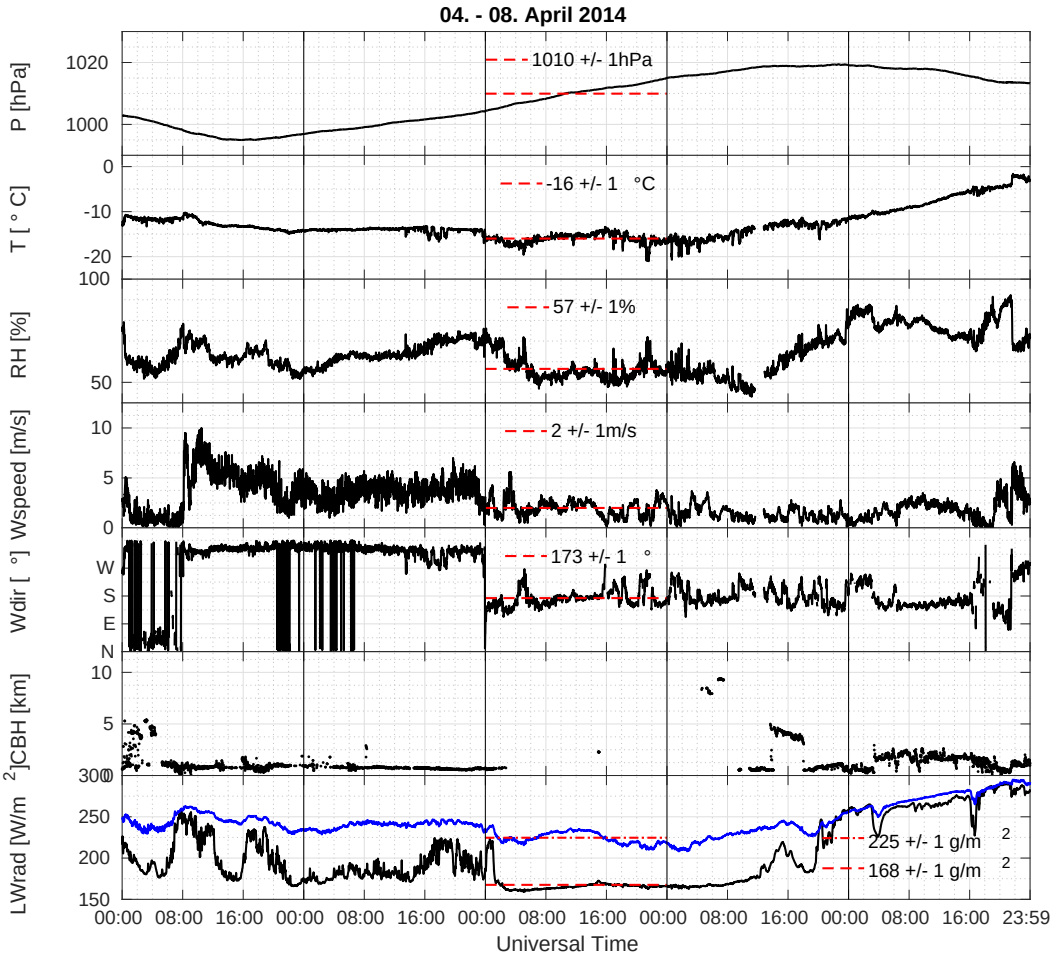

Figure 6: Surface (2 m) pressure, temperature, relative humidity, wind direction and wind speed as well as the lowest CBH from the ceilometer and upwelling (blue line in lowermost panel) and downwelling (black line in lowermost panel) longwave radiation from the BSRN station for April 4th to 8th, 2014 are shown. The red dashed lines indicate the mean with standard deviation for the 6th of April.

The surface pressure indicates the passing of a low-pressure-system (cyclone) on the 4th and high pressure on the 7th and 8th of April. The passing low-pressure-system is accompanied by a persisting cloud layer below 1 km until 3 UT on the 6th, turning wind from north/north-east to north/north-west and an increase in wind speed up to 10 m/s. Temperature is slowly decreasing on the 4th and then constant on the 5th, while relative humidity varies between 50% to 80%.
After 3 UT the 6th of April is found to be cloud-free from ceilometer measurements, apart from clouds from 14:55 until 15:02 at 2,27 km. Wind direction changes to southerly and speed decreases to values around 2 m/s. Temperature on the 6th is lowest in the discussed time span (-16 ± 1 °C) and shows larger fluctuations for this cloud-free day than for the state before with low clouds and higher wind speed. Relative humidity decreases from 70% to an average of 56% ± 6%. Climatological mean temperature and relative humidity for Ny-Ålesund in April are -9°C and 71% (Maturilli et al. (2013)), which makes this day comparatively cold and dry on the surface.
Starting on April 7th, the temperature rises steadily by 15°C throughout the 7th and 8th, while relative humidity rises to over 80%.
In general, the upwelling longwave radiation follows the course of the surface temperature. The downward longwave radiation (LW_{down}) is highly affected by clouds. On the 6th, the average LW_{down} is 168 ± 10 Wm^{-2} standard deviation. It is highly affected by the low-level clouds, especially during the first hour, when liquid-bearing clouds were present (LWP is discussed later on in this section). LW_{down} rises up to 220 Wm^{-2} and decreases back to 160 Wm^{-2} at 1 UT. It decreases further by 10 Wm^{-2} until 3 UT, when the ceilometer detects the last clouds. From there, LW_{down} slowly rises until 15 UT where there is a local maximum. Until the end of the day it remains constant at its mean value.

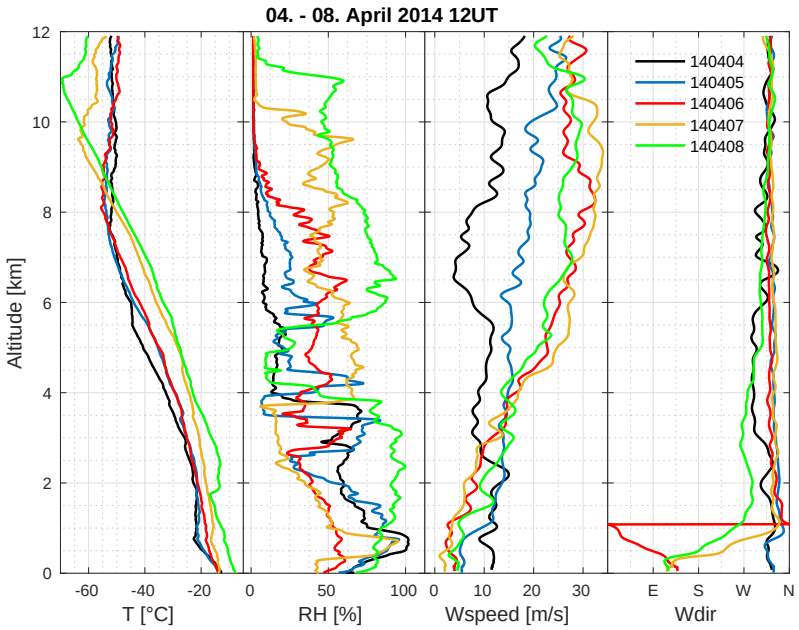

Figure 7: Profiles of temperature, relative humidity, wind speed and wind direction from radio soundings on the 5th (black), 6th (blue) and 7th of April (red) are depicted.

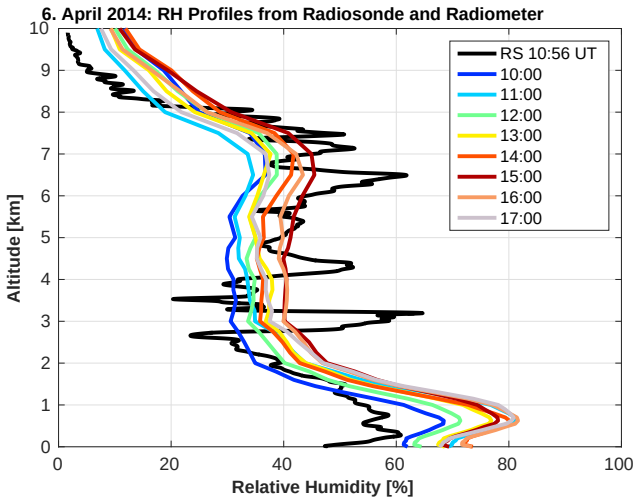

Figure 8: Profiles of relative humidity from radio sounding (black line) and MWR (colored lines) for April 6th are shown.

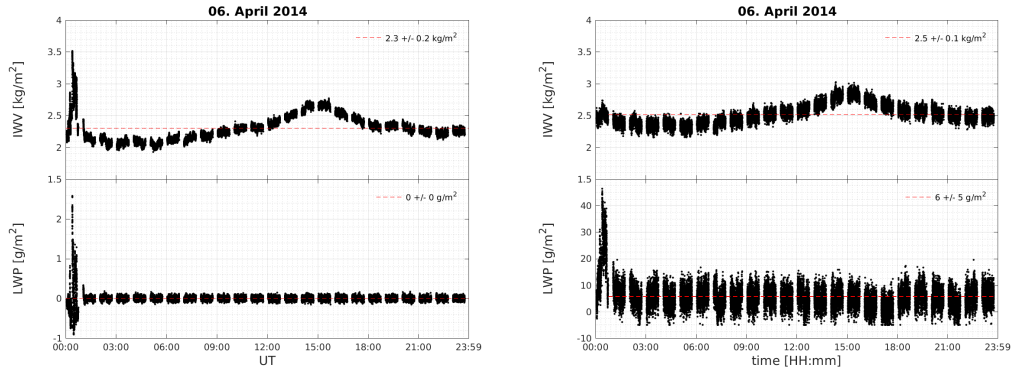

Figure 9: Liquid water path (LWP) and integrated water vapor (IWV) for the 6th of April 2014. Data in the left was processed by colleagues from University of Cologne. Data on the right was processed with the built-in retrieval by Radiometer Physics.

The radio soundings of these days are presented in figure 7. Wind direction is north-westerly in the free troposphere.

Figure 8 depicts relative humidity measured by radio sounding and MWR. It shows that the MWR is only able to reproduce the general structure of the atmospheric humidity profile and that it overestimates the humidity in the lowermost kilometer. However, it shows that the humidity in the troposphere increases, with a maximum at 15 UT.

Figure 9 shows the LWP and IWV from the MWR retrieved with the built-in retrieval by Radiometer Physics on the right and with the retrieval by colleagues from the working group of Prof. Dr. Crewell at the University of Cologne on the left. LWP by Cologne retrieval is zero except for the first hour, where it rises to $3\,\mathrm{gm}^{-2}$, which is below the retrieval uncertainty of $20\,\mathrm{gm}^{-2}$ (Crewell and Löhnert (2003)). The IWV's mean and standard deviation for the 6th are $2.3 \pm 0.2\,\mathrm{kgm}^{-2}$. The first hour shows values of 2-3.5 kgm^{-2}. Between 12 and 18 UT the IWV rises above the mean with a local maximum

of 2.7 kgm^{-2} at 15 UT. The built-in retrieval shows larger noise for both LWP and IWV. LWP is on average $6 \pm 5\,\mathrm{gm}^{-2}$. Since the ceilometer (and also the photometer and the radiation measurements, see the following paragraph) doesn't indicate clouds for most of the day this seems to be a constant offset due to a retrieval error. In addition, this retrieval detects the risen amount of water in the column in the first hour as liquid, whereas the improved retrieval asserts most of the water as vapor. The course between 12 and 16 UT is the same for IWV in both retrievals. In conclusion, surface meteorology, ceilometer and radiometer show that the 6th of April 2014 was a cold, and mostly dry and cloud-free day.

6.2 Aerosol and cloud properties

Since the sky is mostly cloud-free, the aerosol load in the atmosphere can be investigated with data from the sun-photometer. The solar-angle-threshold (5 degrees or higher) sets the starting point of plausible photometer data for this day (at 4:45 UT), the radiation threshold (direct radiation higher than $120\,\mathrm{Wm}^{-2}$) sets the end time (17:21 UT). At 17:18 UT direct radiation decreases to zero within 4 minutes. This indicates shading by mountains.
Figure 10 presents the data from the sun-photometer in two parts, accompanied by shortwave radiation from the BSRN-station. The left image shows the aerosol properties up to the time of beginning cloud influence (about 14:20 UT). Until 12 UT the AOD at 500 nm is almost constant with a mean and standard deviation of 0.086 ± 0.01. At the same time the AE rises from 1.1 to 1.7. This increase of the AE can be explained when looking at the two days before the 6th. Lisok et al. (2016) and Ritter et al. (2016) explored these days extensively. Lisok et al. (2016) found that on the 4th of April 2014 there is an event of high concentrations of sea-salt in the boundary layer, which was produced locally due to an increase in wind speed. They also found high concentrations of mineral dust in the free troposphere at 5 km, coming from northern Russia. On the 4th of April the AE got as low as 0.5 (without cloud contamination). After a low-pressure system passed Svalbard the AE started to rise. Wind speed decreased and therefore the sea-salt production ceased. Also the particle concentration below $1\,\mu$m increased from the 5th to the 7th of April and chemical analysis showed an increase of sulphate(Lisok et al. (2016)).
Hence, the AE increases on April 6th because the size-distribution changes with decreasing number of big sea-salt particles and increasing number of small sulphate aerosols. Beginning at 12 UT the Ångström exponent stabilizes with a mean and standard deviation of 1.74 ± 0.02, which is rather high. The AOD rises from 0.08 to 0.1. This indicates that the size-distribution is retained but the number concentration of small particles increases significantly since at this size (mostly below 0.2 μm diameter) the scattering efficiency is quite low and the AOD rises by 0.03.
Starting at 14:19 UT the AE starts to decrease and the optical depth starts to oscillate. The right part of figure 10 shows the COD in the first panel. A constant AOD of 0.1 is assumed and was subtracted from the optical depth

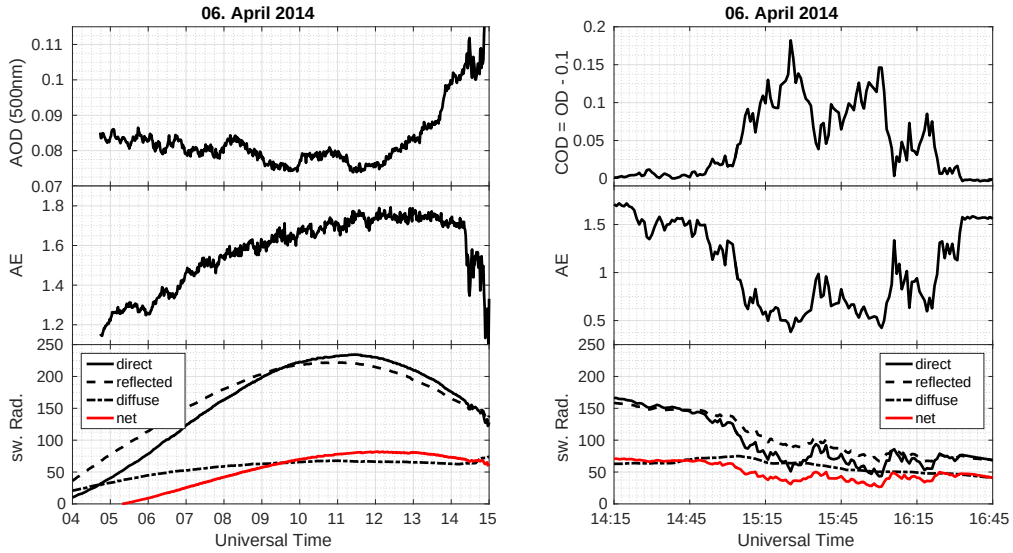

Figure 10: Data from April 6th, 2014 in two parts: Each includes optical depth (first panel) and Ångström exponent (second panel) from sun-photometer, direct shortwave radiation from the Pyrheliometer and diffuse and reflected shortwave radiation from the Pyranometers (third panel). The red line in the third panel is the net shortwave flux. Direct shortwave radiation was multiplied with $sin(\alpha)$ to be referenced to the surface like the other shortwave measures instead of in the sun's direction.

to yield the COD. This AOD seems reasonable, since the COD is around zero between 14:15 UT and 14:45 UT and after 16:34 UT. The AE stays constant at 1.53 after 16:34 UT. In between a thin cloud structure passes in front of the sun. For this period COD and AE show an anti-correlated pattern of three local maxima in the COD (0.18,0.15,0.08) and minima in the AE (0.4,0.4,0.6). The Ångström exponent is not zero, i.e. the extinction is dependent on the wavelength.

Direct solar radiation has the same temporal evolution as the COD. The diffuse shortwave radiation slightly increases with cloud presence. Since diffuse radiation is downwelling shortwave radiation of the entire half sphere except for the direct solar direction, its curve is smoother than the direct radiation. The reflected shortwave radiation decreases with the same temporal pattern, because the reflected radiation is directly linked to the incoming radiation. Although the downwelling radiation increases slightly, the longwave radiation is not influenced significantly.

Questions are now, whether the lidar measurements confirm these optical properties, if they probe the same cloud and what is the geometrical extent of the cloud?

Wind direction and wind speed from the wind lidar are shown in figure 11. The wind lidar has enough tracers to exceed the signal-to-noise-ratio (SNR) threshold up to about 1400 m throughout the day. The wind direction is southeasterly up to about 500 m, where direction turns to easterly and then to northerly. The wind speed is between 0 and 6 m/s up to 1 km. In the hours before 3 UT the wind speed is higher with 10-12 m/s or even higher than 14 m/s. Later on

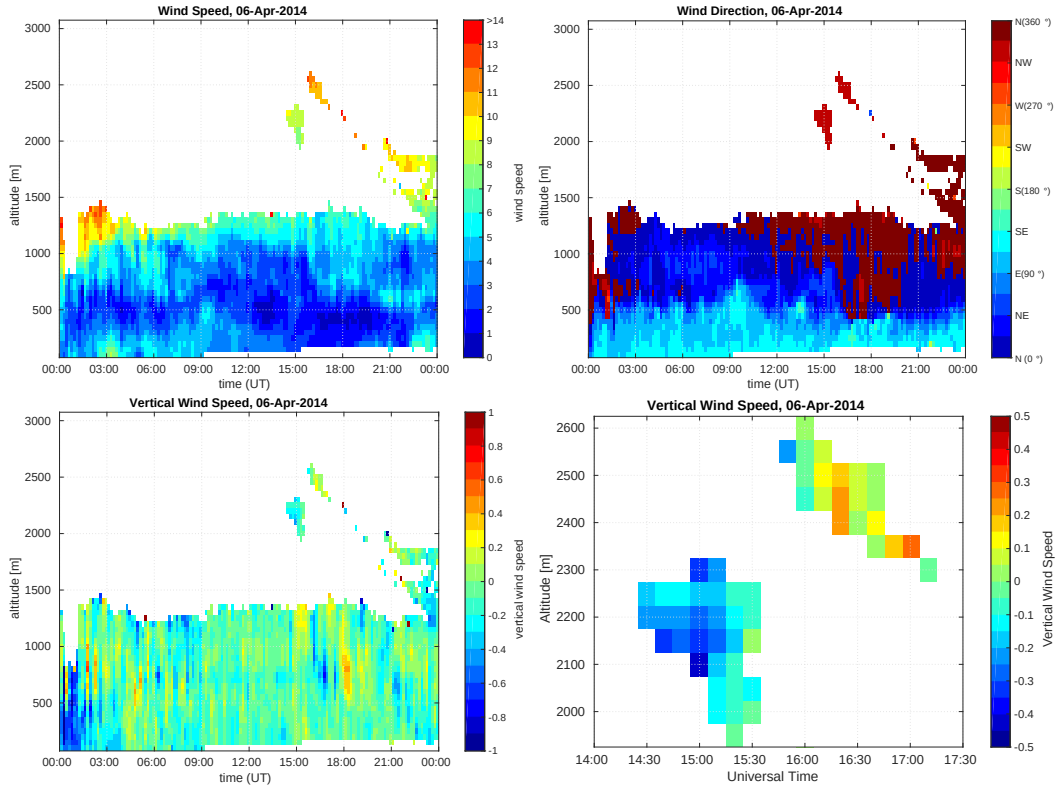

Figure 11: Wind speed (upper left), wind direction (upper right), vertical wind speed (lower left) and zoomed-in vertical wind speed (lower right) from the wind lidar for the 6th of April 2014.

wind speeds calm down.

Between 14:30 and 17:10 the wind lidar has enough tracers between 1950 m and 2600 m. This short period indicates clouds as tracers, because aerosol is expected to be more homogeneous within a few hours. However, it is possible that not all tracers are cloud particles, since the wind lidar is also sensible to smaller particles.

The first cloud, according to the wind lidar, passes between 14:30 and 15:30 UT with decreasing CBH from 2200 m to 1950 m. The mean wind speed is 8 m/s for an hour. Assuming clouds moving with the wind, this yields a maximum horizontal extent of the cloud in wind direction of 28 km.

A second cloud structure is detected by the wind lidar between 15:50 and 17:10 UT. CBHs are still decreasing with time from 2550 to 2300 m. The cloud structure is higher in altitude and the mean wind speed is also higher with 11 m/s.

The general height agrees with the ceilometer which gives CBHs of 2260 m up to 2290 m, but the ceilometer gives these CBHs only between 14:55 and 15:02 UT.

The vertical wind speed in figure 11 shows mostly small values around zero. The clouds before 3 UT have an upward motion. The zoomed image of the two clouds in the afternoon in figure 11 reveals movement in opposing directions. The first and lower cloud has an upward movement while the second, higher one has a downward movement.

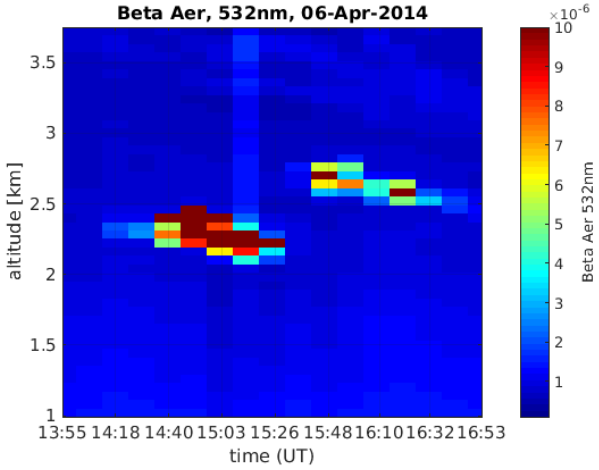

Figure 12: Total backscatter at 532nm from KARL: zoom on the thin clouds in the afternoon of the 6th of April. Here an image-plot is used instead of a contour-plot to see the actual cloud boundaries at the measured height and time.

UT	α (°)	sun dir (°)	CBH (m)	Wdir (°)	Wspeed (m/s)	dist (km)
14:30	13.8	230 (SW)	2150	322(NW)	8	8.8
15:30	11.4	245 (SWW)	2000			9.7
15:50	10.5	250 (SWW)	2550	327(NW)	11	13.8
17:10	6.8	270 (W)	2300			19.3

UT	α (°)	sun dir (°)	CBH (m)	CT (m)	max. COD	dist (km)
14:29	13.9	230 (SW)	2280	480	0.18	9.2
15:26	11.6	244 (SWW)	2040			9.9
15:37	11.1	247 (SWW)	2640	360	0.02	13.5
16:32	8.6	261 (W)	2520			16.6

Table 1: Two time and height intervals of clouds were deduced from the wind lidar (top table) and KARL backscatter (bottom table). The tables give the deduced time intervals in Universal Time (UT), the calculated sun elevation angles (α) and azimuth angles (sun dir) at that times, cloud base heights (CBH) that were deduced from the respective measurement. The upper table gives the mean wind direction and mean speed in the time-height-interval. The lower table gives the geometrical cloud thickness (CT) and the maximum integrated Raman Alpha, which equals cloud optical depth (COD) in the time-height-interval. The last column gives the distance between an air parcel in sun's direction at CBH and an air parcel at CBH in zenith-direction for the respective sun angles: dist = CBH/tan(α).

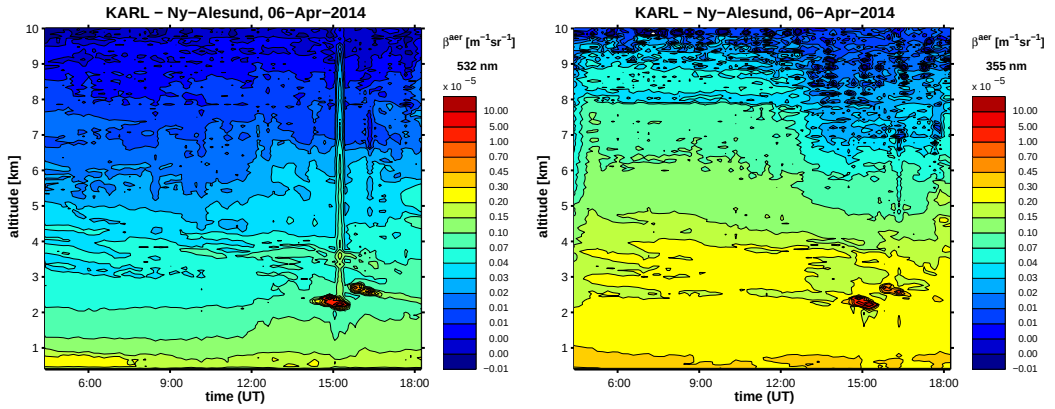

Figure 13: Total backscatter from KARL: full measurement period on the 6th of April for 532nm (left) and 355nm (right). Notice the effect of multi-scattering at 532nm which distorts one profile, so that it seems that scattering is raised up to 10 km, but in reality this delay is caused by multiple scattering inside the cloud. This means that the actual backscattering value inside the cloud is higher and above the cloud it should show values similar to the neighboring profiles. *Figures are courtesy by Christoph Ritter.*

Table 1 also gives the cloud extent deduced from the backscatter signal of KARL by visual examination of backscatter at 532 nm (see figure 12). CBHs of the wind lidar and KARL agree well, within 130 m, which is about two height bins. The "starting" edge of the cloud in wind direction is deduced from figure 12 to be at 14:29 ± 11 minutes uncertainty and cut-off in wind direction at 15:26 UT. This agrees well with the boundaries from the wind lidar. Vertical extent is estimated to 480 m ± 120 m.

It is also possible to calculate the cloud optical depth from the KARL lidar. Extinction profiles are retrieved with the Raman method for 532 nm and 355 nm. Extinction at 355 nm is shown in figure 14 (532 nm looks similar, not shown). Integrals for each extinction height profile over the cloud area minus the aerosol background (area at same height for four time-steps before the cloud area) yield the cloud optical depth (COD) for each time step, see figure 15. The first cloud's extent based on high COD is 14:40-15:26 UT, the second cloud's extent is 15:37-16:32. One should keep in mind, that KARL integrates for 10 minutes. That means that each data point represents the state of the atmosphere within the altitude grid for the past 10 minutes. The maximum COD of the first cloud is 0.18 and was measured by KARL at 14:52 UT. The second cloud has a maximum COD of 0.02, which is in the subvisible range. The photometer also registered a maximum COD of 0.18 at 15:25. This similarity suggests that both probed the same cloud. The wind direction is roughly 325° and sun's direction is 244° at 15:25 UT. This means that if a cloud band was to move in the wind direction that was measured by the wind lidar in Ny-Ålesund, it would have been in the photometer's field of view before it reaches zenith over Ny-Ålesund. In conclusion, either the clouds did not move with the wind or the lidar and the photometer did not probe the same cloud. The cloud integrated backscatter (CIB) shows two peaks, at 14:52 UT and 15:14 UT (see figure 15). The values of the CIB are twice as high for 355 as for 532 nm at 15:14 UT. This is partly due to the multiple-scattering which

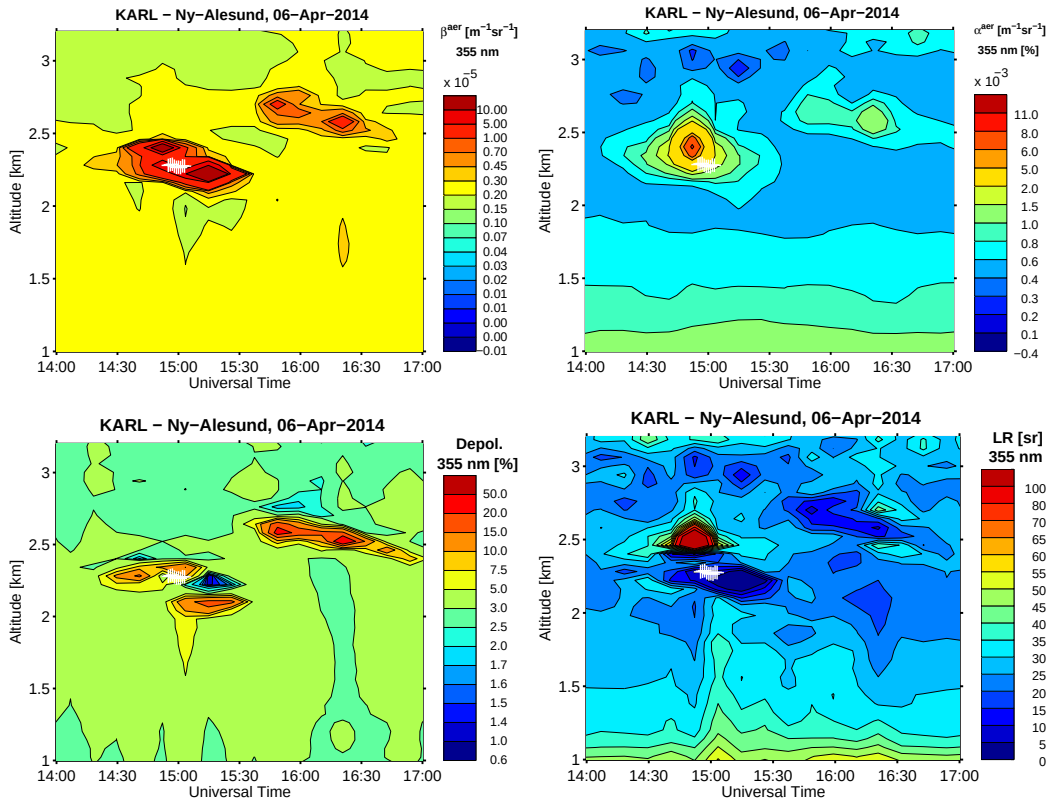

Figure 14: Backscatter at 355 nm (upper left), extinction at 355 nm (upper right), particle depolarization at 355 nm (lower left) and Lidar Ratio at 355 nm (lower right) from KARL for 14-17 UT on the 6th of April. The white cross symbols indicate the cloud base heights derived from the ceilometer.

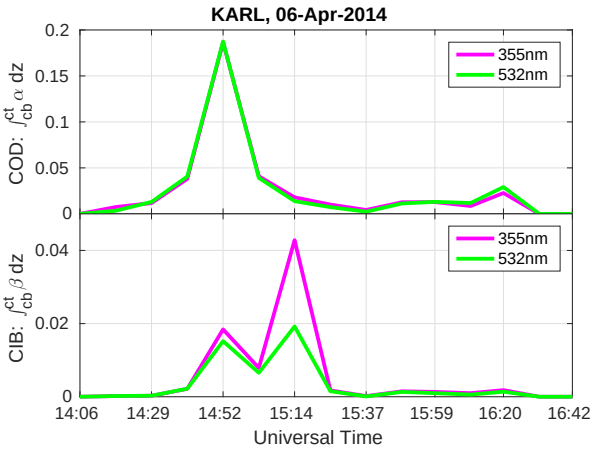

Figure 15: Profiles of extinction were retrieved with the Raman method for 532 nm (green) and 355 nm (magenta). The integral for each height profile over the cloud area minus the aerosol background (area at same height for four time-steps before the cloud area) yields the cloud optical depth. The same procedure for backscatter at 532 nm and 355 nm gives the cloud integrated backscatter (CIB).

occurred for this time-step. This can be seen in figure 13, as for this time step the atmospheric profile of backscatter is distorted towards bigger values above the cloud up to more than 9 km while the 355 nm does not show this distortion. Therefore, the amount of backscatter in the cloud area is underestimated for 532 nm. The integrated extinction COD shows no dependency on wavelength. This is unexpected because the AE determined by the sun-photometer is larger than zero, which means that the extinction has a wavelength dependency in the sun's direction. However, the AE from the sun-photometer is contaminated with the aerosols behavior. To yield an AE of clouds, one would have to subtract the individual AOD at each wavelength and then derive the AE. This is a suggestion for future studies.
The particle depolarization is shown in figure 14. It reveals that both clouds are made of mixed phase. Using the definition of an ideal mixed-phase cloud with a water layer above ice (c.f. Morrison et al. (2011)), the first cloud can be divided into two parts with water (low Depol.) above ice (high Depol.).
The ratio between extinction and backscatter (called LR) is given in figure 14 as well. The LR reaches very high values above the first cloud and low values within the cloud. The second cloud is indistinguishable from the background. The cloud base heights reported from the ceilometer are symbolized with white crosses in all four parts of figure 14. They do not match the cloud base from KARL and are systematically too high.

6.3 Cloud radiative forcing

The cloud radiative forcing is shown on the left in figure 16. Clear sky radiances were estimated to be the respective net flux from the times right before and after the cloud with a linear interpolation in between. The shortwave cloud radiative forcing (upper panel in figure 16) is negative and reaches peak values of -27, -26 and -15 Wm^{-2}. The longwave CRF (middle panel on the left in figure 16) is negligible. The net cloud radiative forcing is negative with a maximum of -25 Wm^{-2}. Hence, the shortwave radiation is influenced significantly at this low solar angle.

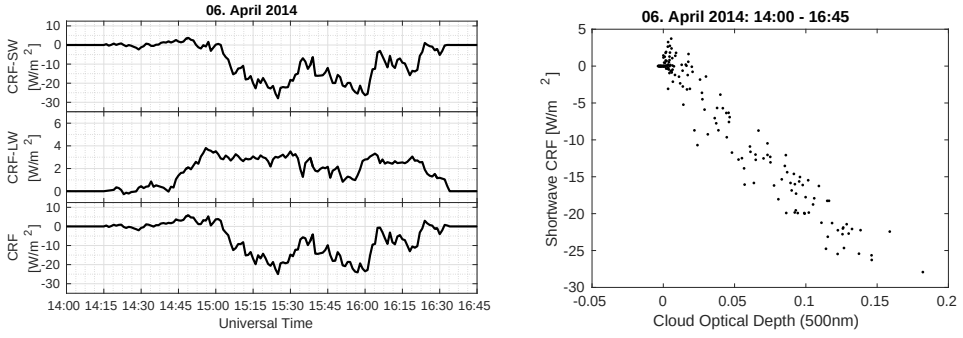

Figure 16: Left: Cloud radiative forcing for shortwave radiation. The cloud-free sky radiative forcing was estimated to follow the net shortwave fluxes until 14:15 UT and from 16:34 UT on. A linear interpolation was used in between. Right: Shortwave cloud radiative forcing over cloud optical depth from the sun-photometer at 500 nm.

The right image in figure 16 illustrates the linear correlation of shortwave CRF

and optical depth from the sun-photometer. This is consistent with the results from Dupont and Haeffelin (2008).

6.4 Summary

The clouds investigated here are short-lived (up to 1.5h), according to all instruments, and have a small vertical (up to 400m) and horizontal extent. The small extent, the wavelike structure in the photometer data and the opposing vertical wind directions suggest that the clouds registered by those instruments were induced orographically (Lee-clouds). The clouds observed on this day have a small optical thickness up to 0.18 and are composed of liquid as well as ice particles. The amount of backscatter is wavelength dependent and the maximum of extinction is located at the top of a cloud. The effect on the longwave radiation is negligible. The shortwave radiation is reduced by up to $25\,\mathrm{Wm}^{-2}$ which corresponds to a reduction by more than 30% at this low sun angle. It was also shown that the ceilometer does not report sub-visible clouds (COD<0.03).

7 Case study: 8th of May 2015

Measurement results from the atmospheric observatory at AWIPEV station in Ny-Ålesund on May 8th, 2015 are presented in this chapter. First, the general weather situation is described. Then, the aerosol load on this day is characterized and subsequently properties of the clouds measured on this day are presented. Particularly, geometrically thick clouds during mid day are investigated in detail. Following up, two methods to derive the cloud radiative forcing (CRF) are applied to this day and the results are compared. Finally, the findings are summed up.

7.1 Weather situation

The weather situation on May 8th and two preceding and two succeeding days is discussed on the basis of basic surface meteorology, cloud base height (CBH) and longwave radiation (see figure 17).

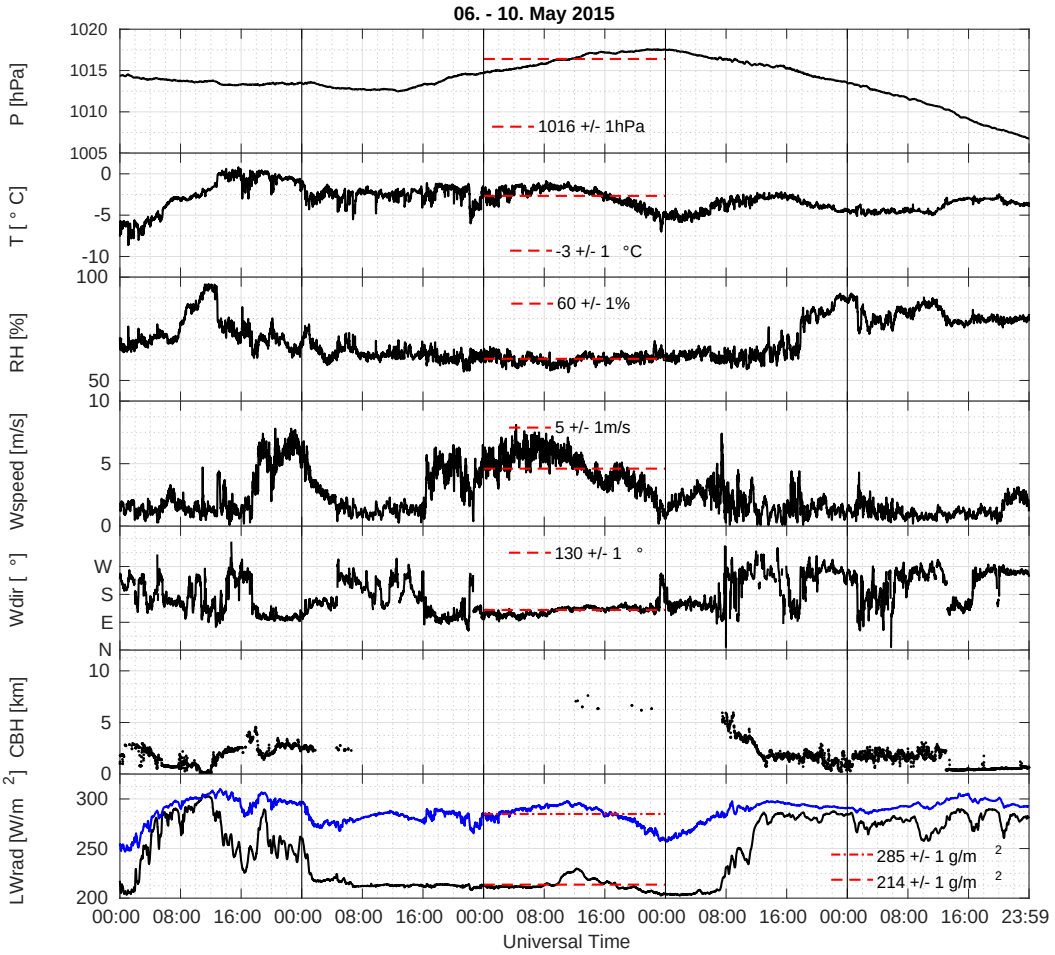

Figure 17: Top to bottom: surface (2 m) pressure, temperature, relative humidity, wind direction and wind speed as well as lowest CBH from ceilometer and upwelling (blue line in lowermost panel) and downwelling (black line in lowermost panel) longwave radiation from BSRN station for May 8th, 2015. The red dashed lines indicate the mean, which is given with the value ± standard deviation for May 8th.

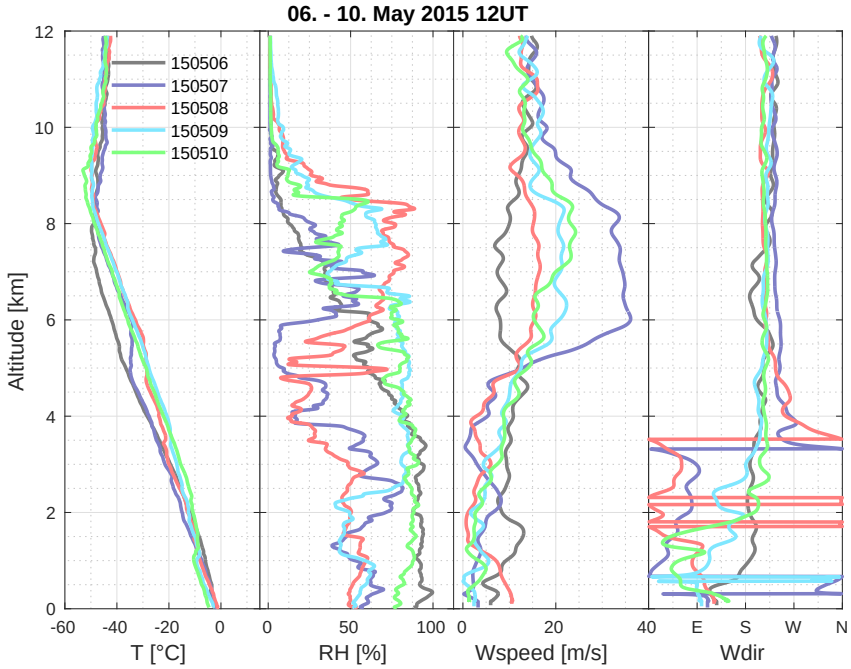

Figure 18: Left to right: Profiles of temperature T, relative humidity RH, wind speed Wspeed and wind direction Wdir from radio soundings on May 8th, 2015 (red) and two days before and after (colors given in the legend).

The surface pressure course of the five days can be divided into three parts. The first part is characterized by almost constant pressure until noon of the 7th of May. Then, pressure increases until the end of the 8th of May. Thereafter, the pressure decreases noticeably. The surface temperature increases strongly by eight degrees during the first half of May 6th and reaches thawing temperature for a few hours. Subsequently, it fluctuates between -6 and -2 degrees Celsius. On May 8th the temperature remains fairly constant until noon and then decreases until the end of the day. The mean temperature on May 8th is -3° C which matches the climatological mean for May in Ny-Ålesund (Maturilli et al. (2013)). The relative humidity hints to precipitation at mid day on May 6th. May 8th has a mean relative humidity of $60 \pm 1\%$. This is dryer than the climatological mean of 75% for May (Maturilli et al. (2013)). The ground wind features moderate easterly winds from the evening of May 6th until the morning of the 7th and from the evening of the 7th until the end of 8th of May. The ceilometer reports mid to low altitude clouds on the 6th of May which strongly affect the downwelling longwave radiation. The cloud cover opens up during the morning of May 7th and the sky remains clear until noon on May 8th. Then, broken high clouds occur on May 8th which slightly affect the downwelling longwave radiation. These are the clouds studied in this chapter. On the next day, the cloud base height decreases until noon and net longwave radiation decreases. Hereafter, clouds occur at varying height below 3 km until noon of May 10th. Thereafter, low clouds cover the sky with a constant CBH. The upward longwave radiation generally follows the course of the surface temperature.

Noon radio soundings (depicted in figure 18) reveal a warming trend of the

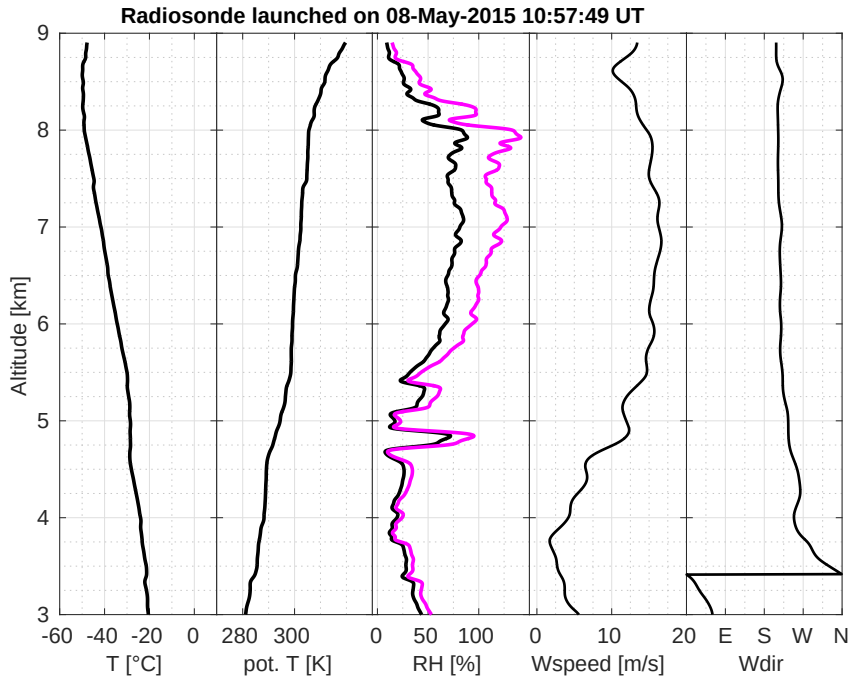

Figure 19: Left to right: Profiles of temperature T, potential temperature, relative humidity RH over water (black) and over ice (magenta), wind speed Wspeed and wind direction Wdir from radio sounding on May 8th, 2015.

troposphere from top to about 1 km in steps in the course of the five days studied, while below 1 km the opposite trend can be observed. Humidity above 4 km altitude shows high variability. The above described cloud cover on May 6th, 9th and 10th match with high levels of relative humidity. Wind above 4 km comes from south-westerly direction during all five days but with variable speed. Between 1 and 3 km, wind direction is more influenced by the terrain. Wind brings warm and moist air from the south on May 6th. On May 7th, the wind direction has changed to northerly winds. On May 7th and 8th, the wind direction changes between 3 and 4 km from east over north to southwest.
A closer look on the profiles of May 8th is taken in figure 19. The radiosonde on this day was launched at 10:57 UT and reached 10 km at 11:32 UT. The potential temperature is stable between 4.6 and 5.5 km (i.e. it has a positive slope) and weakly stable (i.e. small positive slope) between 5.5 and 8 km. In the stable altitudes the air cannot mix well. At 4.7 to 4.8 km the radiosonde passes a wet layer with relative humidity over ice close to 100%. Between 6 and 8 km the relative humidity over ice exceeds 100% with local maxima of 128% at 7.1 km and 142% at 7.1 km. The wind speed increases between 3.7 km and 6 km. Between 6 and 8 km the wind speed is fairly constant.

7.2 Cloud properties

Figure 20 shows the backscatter and volume depolarization at 355 nm from KARL on May 8th, 2015. The data was kindly provided by Christoph Ritter, since this day was difficult to process. It required several iterations of processing and adjusting the parameters, because of high levels of noise in the 532 nm

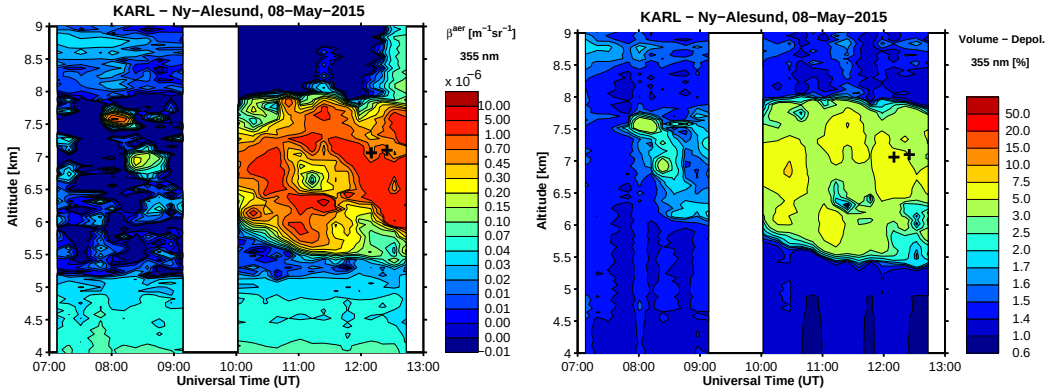

Figure 20: The contour plot on the left shows backscatter at 355 nm from KARL for May 8th, 2015. The contour plot on the right shows volume depolarization at 532 nm. Overlayed on both are black plus symbols which indicate cloud base height reported from the ceilometer. The white space indicates a data gap.

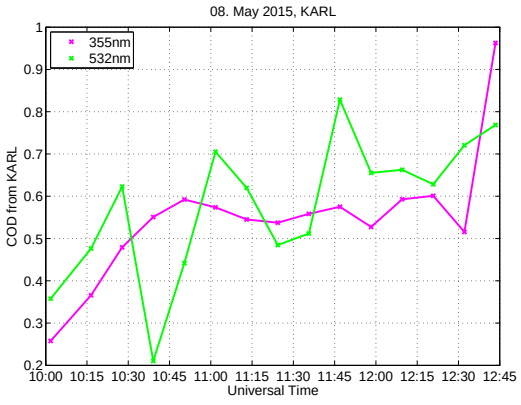

Figure 21: Cloud optical depth at 532 nm (green) and 355 nm (pink) is shown. Extinction, calculated from Raman channels, was integrated over the cloud area, minus the integrated aerosol background beforehand.

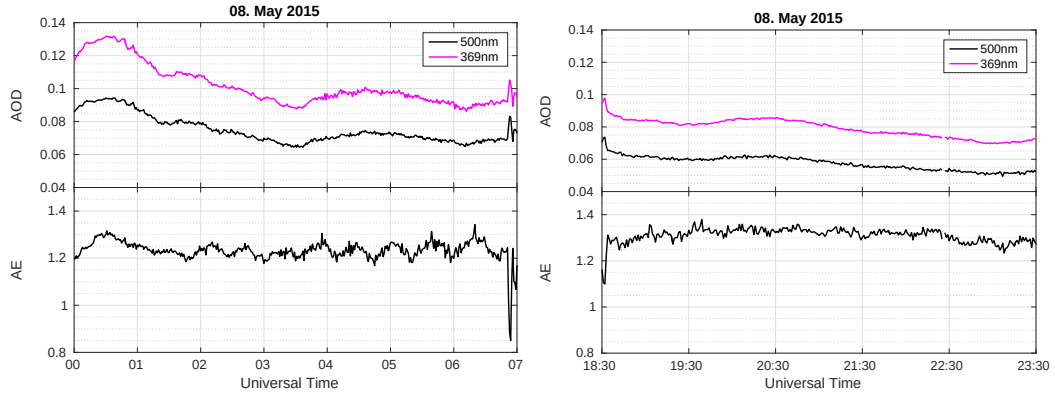

Figure 22: Aerosol optical depth (AOD) at 500 nm (black) and 369 nm (magenta) and Ångström exponent (AE) from the sun-photometer before the cloud (left) and after the cloud (right).

channel and in the Raman channels and due to multi-scattering inside the cloud. There is a data gap between 9 and 10 UT, because KARL was set to stand-by for a correction of the overlap. At 12:48 UT KARL was shut off for the day. This was probably due to the increasing amount of multi-scattering inside the cloud, which can be seen in the last time step above the cloud in the backscatter at 355 nm.

Backscatter in both 532 nm (not shown) and 355 nm (left image in figure 20) indicates a cloud structure of more than 2 km geometrical thickness between 10 UT and 12:45 UT at altitudes 5.5 km to 8 km. This altitude is consistent with the measurement of more than 100% relative humidity over ice in the radio sounding profile from this day (see figure 19). Figure 20 also depicts the cloud base height reported minutely from ceilometer as black crosses. It can clearly be seen that the ceilometer misses a lot of ice over time and space. The reported height seems to be arbitrary in the cloud. This suggests that the proprietary CBH detection algorithm integrates the profile until a certain threshold is reached where the CBH is set. Deriving CBH from one wavelength backscatter could be done by combining two conditions: A sharp increase in the derivative of backscatter over height combined with a check for average backscatter above this height and below this height. With two wavelengths, the color ratio could be used as a cloud detection condition since high color ratio indicates aerosols and low color ratio indicates clouds (as done in my previous report on processing data from airborne lidar, c.f. Kautzleben (2016)). However, the cloud is probably too high and too thin for the ceilometer due to the comparatively weak laser pulse and resulting low signal-to-noise ratio.

The cloud structure is heterogeneous in backscatter, both in the visible and UV wavelength. Volume depolarization (right image in figure 20) ranges between 0.03 and 0.10. Chen et al. (2002) investigated 10 years of lidar detected high ice clouds (cirrus) and found an average depolarization of 0.3. Furthermore, they found that for clouds between 0.1 and 1 COD the volume depolarization is lower than for cirrus with COD<0.03 (subvisible cirrus). Therefore, a depolarization of 0.03-0.1 is within the range of results of Chen et al. (2002). The low depolarization can be explained with e.g. hexagonally shaped ice crystals. The cloud is almost purely made of ice, except for a small area at 11:24 UT at 6.3 km where low depolarization in this height and reduced backscatter above suggest existence of water. The microwave radiometer detects no liquid on this day (not shown).

The lidar ratio is not depicted since the noise is too high to resolve the structure of the cloud, the mean lidar ratio inside the cloud is 14 ± 4 (estimated error from noise). This is comparatively low for a cirrus. Chen et al. (2002) found an average lidar ratio of 29 ± 12 for tropical cirrus clouds. However, they found that the average lidar ratio decreases with height. Thus, the values of depolarization and lidar ratio are comparatively small, but reasonable.

Figure 21 shows the COD derived from the integration of extinction at 355 nm (UV, magenta line) and 532 nm (visible, green line). The COD increases from 10 UT to 11 UT and then remains almost constant until 12:30 UT at 355 nm, but seems to have an increasing trend at 532 nm with high level of noise.

In the following, the AOD of the sun-photometer is discussed. An estimate of

the background AOD is needed to estimate the COD from the sun-photometer. Thereafter, the COD derived from KARL and from the sun-photometer are compared.

Aerosol measurement results from the sun-photometer from cloud-free times of May 8th are shown in figure 22. The AOD is slowly decreasing over the course of the day from 0.13 to 0.07 at 369 nm and from 0.09 to 0.05 at 500 nm. Judging from the amplitude of the AOD and AE, clouds are in the sun-photometer's field of view between 6:52 UT and 18:34 UT. During this time, the AOD is assumed to be constant at 0.07 ± 0.02 at 500 nm and 0.09 ± 0.02 at 369 nm. This assumption is reasonable since the AOD usually changes slowly over hours and a large increase would still be visible after days. Moreover, the COD is a magnitude larger than the AOD, so that an AOD $\pm$ 0.02 is still good assumption for estimating the COD. The AE of the aerosol background shows no trend and varies between 1.2 and 1.3.

The resulting COD from the sun-photometer is shown in the top panel of figure 23. Both COD at 500 nm and at 369 nm show similar temporal progression. In the morning (around 7:30 to 9 UT) and in the afternoon (around 15:45 to 16:46 UT) clouds with a COD of up to 0.2 cross in front of the sun and affect the direct and diffuse radiation (third panel in figure 23). The clouds at mid day are more prominent. The COD starts increasing at 11 UT and peaks at 11:30 UT with 0.6, then decreases until 3 UT with temporary increases to 0.4 in between.

AE (shown in the middle panel in figure 23) is reduced well below 0.5 for the above mentioned clouds in the morning, mid day and afternoon. This low AE indicates large particles.

Downwelling longwave radiation (fifth panel in figure 23) and diffuse shortwave radiation (third panel in figure 23) show similar temporal evolution. The diffuse shortwave radiation increases because of the increased scattering by the clouds. Downwelling longwave radiation increases due to the higher emission by clouds in the infrared range. Direct shortwave radiation is anti-correlated to the COD, because the COD is derived from the transmittance at distinct wavelengths and direct radiation is transmitted shortwave radiation at broadband wavelengths. The upwelling longwave radiation (fourth panel in figure 23) shows similar temporal evolution as the upwelling shortwave radiation (third panel in figure 23) but with a much smaller amplitude. The upwelling shortwave radiation is directly linked to the downwelling shortwave radiation via the albedo, therefore it follows the downwelling curve, except for the albedo change due to the melting of snow. The upwelling longwave radiation follows the ground's temperature. Less incoming solar radiation lets the surface cool down and therefore the upwelling longwave radiation also follows the downwelling shortwave radiation but with a smaller amplitude. The time of the reported CBH from the ceilometer (lowermost panel in figure 23) are arbitrary compared to the radiation measurements, i.e. no correlation between high COD and reported CBH can be observed.

Comparing the temporal course of the COD from KARL (figure 21) with the COD from the sun-photometer (top panel of figure 23) reveals that the clouds were detected first in zenith direction and later in (southerly) direction of the

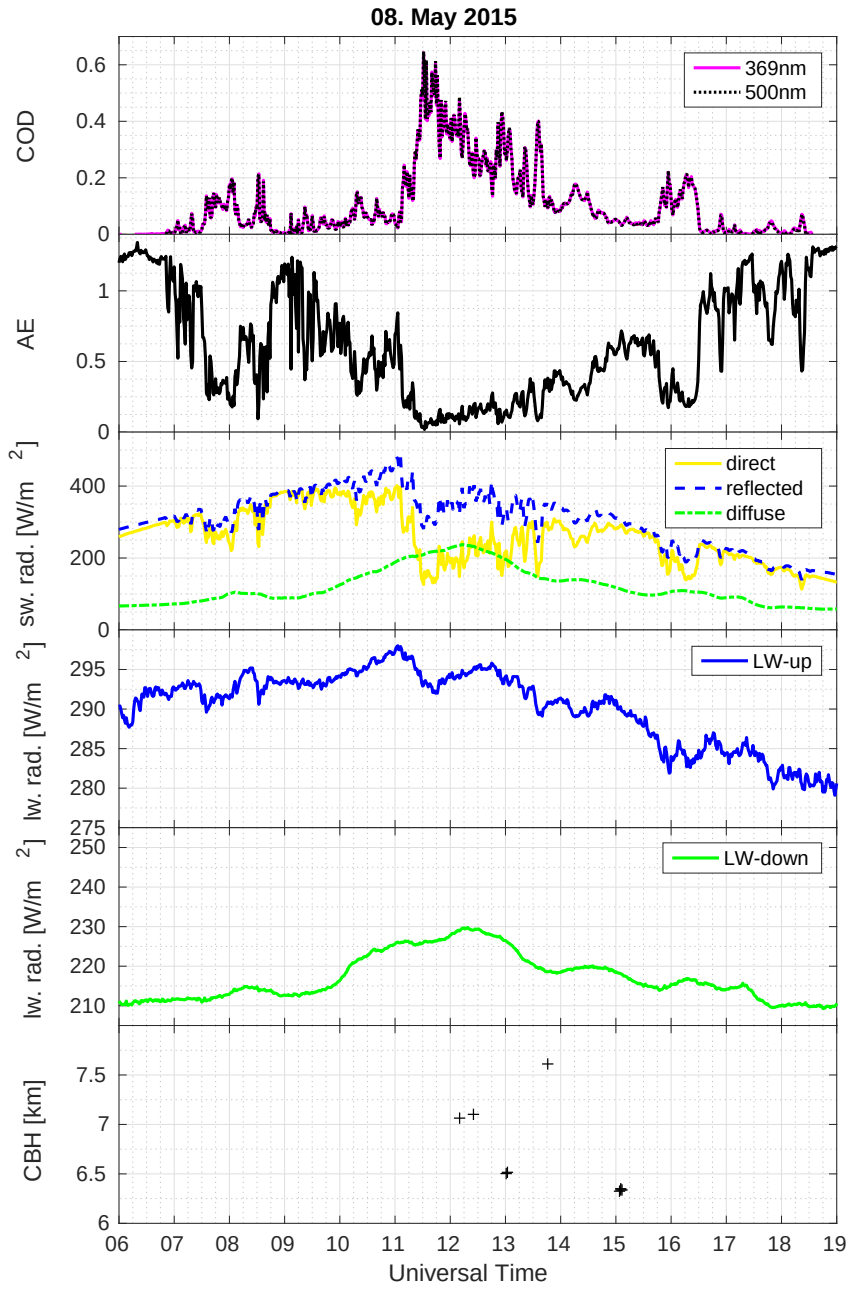

Figure 23: The cloud optical depth (COD) from the sun-photometer is shown in the uppermost panel for the two wavelengths closest two KARL's wavelengths 532 nm and 355 nm: COD(500 nm)=AOD(500 nm)-0.07 and COD(369 nm)=AOD(369 nm)-0.90. The Ångström exponent (AE) is given in the second panel. Shortwave radiation is depicted in the third. Upwelling and downwelling longwave radiation are given in the fourth and fifth panel, respectively. The lowermost panel illustrates the cloud base height (CBH) from ceilometer.

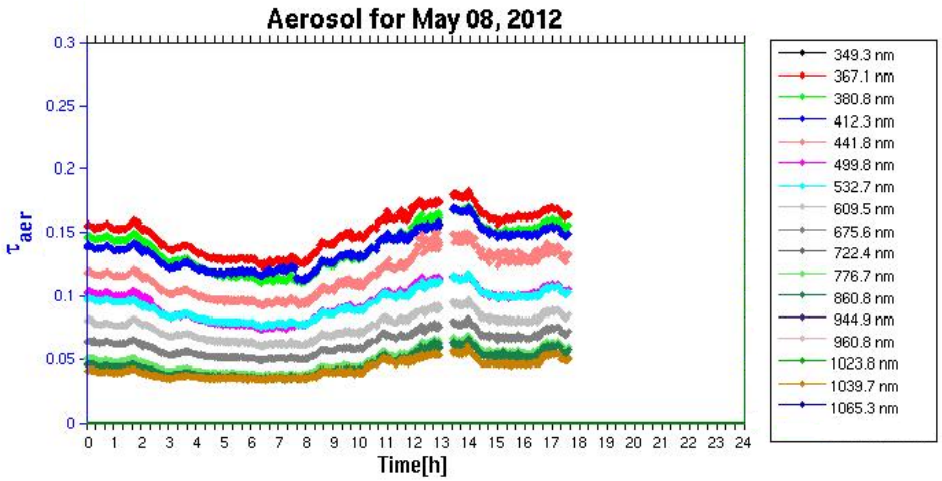

Figure 24: AOD derived from the sun-photometer at seventeen wavelengths from UV over visible to near-IR on May 8th, 2012. *Figure is courtesy of Siegrid Debatin.*

sun. This may be explained by an approaching warm front from the south which is lifted upwards as it flows onto the cold air. In flow direction cirrus clouds form first and later CBH decreases over the measurement site.

7.3 Estimation of the CRF from measurements

Clear sky radiances with similar course of solar elevation and azimuth angle are needed to estimate the shortwave cloud radiative forcing for a specific day. In this case, it is not possible to fit the clear-sky radiance linearly from directly before and after the cloud, as done in the previous case study, since the clouds affect the shortwave radiation for almost 10 hours. Therefore, measurements from the same day three years earlier, May 8th, 2012, which was nearly cloud-free between 0 UT and 18 UT, are used as the reference clear sky radiances. Figure 24 depicts the AOD on this day. This figure is a good example of aerosols affecting the shorter wavelengths more than the longer ones. In comparison to May 8th, 2015, this day has a higher AOD with values at 500 nm between 0.07 and 0.11. Hence, the difference of AOD between the two days gives the opportunity to examine the aerosol radiative forcing in addition to the cloud radiative forcing.

Figure 25a shows the shortwave radiation on May 8th, 2015 (colored lines) and on May 8th, 2012 (dashed black lines). Looking closely, it is revealed that the diffuse radiation at cloud-free times is higher in 2012 than on the same day in 2015 and the direct radiation and reflected radiation are lower than in 2015. The comparatively larger AOD in 2012 reduces the amount of direct radiation reaching the surface and increases the diffuse radiation due to scattering and absorption by a larger amount of aerosols compared to 2015. The lower reflected radiation can be explained by a lower albedo, caused by less snow or darker colored snow. The amount of radiation difference between the 8th of May 2012 and 2015 can be compensated by artificially enhancing and reducing the amount of radiation of the 8th of May 2012. It was found

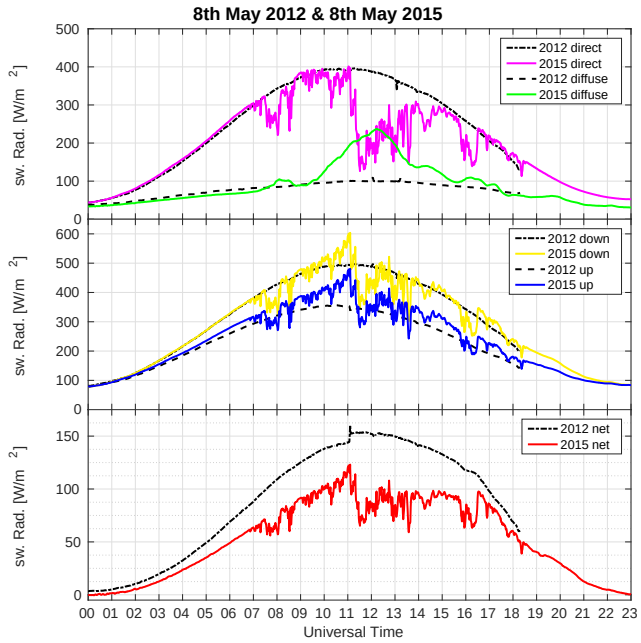

(a) Radiation on 8th of May 2012 is unchanged.

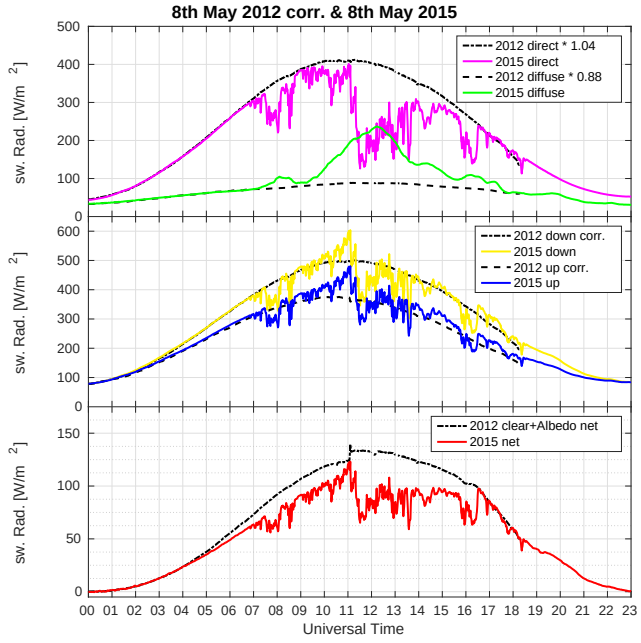

(b) Radiation on 8th of May 2012 was adjusted.

Figure 25: Both (a) and (b) show shortwave radiation on the 8th of May 2015 (colored lines) and on 8th of May 2012 (dashed black lines). The measured direct radiation was multiplied by sine of the solar elevation angle to be with respect to a plane parallel to the ground. The solar elevation angle was calculated with an online tool by U.S. Navy. 'Down' refers to the sum of downgoing direct and diffuse radiation, 'up' denotes the reflected radiation, 'net' equals the difference of 'down' minus 'up'. (a) depicts the original data. In (b) direct and diffuse and reflected shortwave radiation of 8th of May 2012 were multiplied by factors (see legend). The factors were chosen so that the radiation of both May 8th, 2012 and 2015 match best at cloud-free times. The reflected radiation was adjusted as explained in the text.

that radiation of both the 8th of May 2012 and 2015 match best at cloud-free times, when reducing the diffuse radiation by 12±2% and enhancing the direct radiation by 4±1% (compare figures 25a and 25b). To compensate the changed amount of downwelling shortwave radiation, the reflected radiation was added with the difference between the corrected downwelling and the uncorrected downwelling radiation times the original albedo. The aerosol shortwave forcing is the difference between the corrected and the uncorrected net radiation. It is at largest -2.5 W/m^2 and the maximum error adds up to $6\,W/m^2$. Thus, although the error is large, the direct effect of a change in AOD of 0.02 acts cooling in the shortwave radiative forcing.
To get the reference clear-sky net radiation, the difference in albedo has to be accounted for. Hence, 4±1% of the reference clear-sky downwelling shortwave radiation were added to the reflected radiation to simulate a 4% higher albedo. At local noon on the 8th of May 2012 (approx. 11:09 UT) the amount of reflected radiation decreases by $8\,W/m^2$. This is possibly due to a change of the solar angle combined with a non-uniform surface. This change remains uncorrected in figure 25b and adds to the shortwave radiation error as $\pm\,4\,W/m^2$.
Now, after considering the direct aerosol radiative forcing, the shortwave CRF can be deduced from the difference between the reference radiance on May 8th, 2012 minus the time-steps with cloud influence on May 8th, 2015. Later on, this manner of determining the CRF is referred to as the measurement comparison method. The resulting shortwave CRF is depicted the uppermost panel in 29a. The shortwave CRF peaks at -70 W/m^2 around 11:30 UT and 13:30 UT. The error is at most $\pm\,4\,W/m^2$ (direct) $\pm\,2\,W/m^2$ (diffuse) $\pm\,5\,W/m^2$ (reflected) $\pm\,4\,W/m^2$ (reflected). Since these errors are all independent from another, the total uncertainty adds up to $15\,W/m^2$.
The longwave radiation on May 8th, 2012 is not suited as a reference for May 8th, 2015, since the surface temperature was lower on average and had a different temporal evolution. Therefore the clear sky forcing is fitted under the assumption, that upwelling longwave radiation is diminished and downwelling longwave radiation is enhanced by the clouds. The resulting longwave cloud forcing is depicted in the middle panel of figure 29a. It peaks at $22\,W/m^2 \pm 6\,W/m^2$ (error estimated from noise in the longwave CRF in the morning).
The resulting total CRF is shown in the lowermost panel of figure 29a. Overall, the clouds have a negative forcing with peak values of -48 W/m^2 and -53 $W/m^2 \pm 21\,W/m^2$. The positive forcing at 11 UT results from the high impact on the longwave forcing and no impact on the shortwave forcing, since the cloud was in zenith over the measurement site without blocking the shortwave radiation. However, the amount of positive forcing is smaller than the overall uncertainty.

7.4 Estimation of the CRF from a simple model

The simple model by Shupe and Intrieri (2004) described in section 4.8.1 is applied on May 8th, 2015 in Ny-Ålesund and compared to the measured results hereafter.
The downwelling shortwave radiation is simulated with the sine of the solar elevation angle (obtained from an online tool by the U.S. Navy) times the

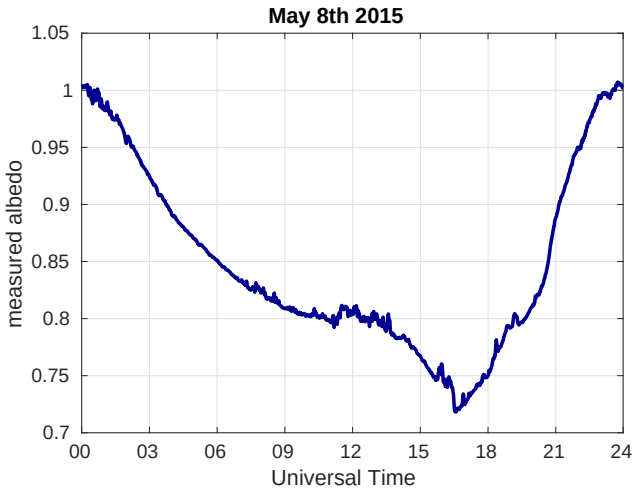

Figure 26: Depicted is the measured albedo=SW_{down}/SW_{up} on May 8th, 2015.

solar constant, which gives the incoming solar radiation at the top of the atmosphere. Multiplying this by the broadband atmospheric shortwave transmission t_{aSW} yields the incoming shortwave radiation at the surface. t_{aSW} is related to the broadband atmospheric optical depth OD by $t_{aSW} = exp(-OD)$. With OD=0.31 the modeled radiation matches the measured downwelling shortwave radiation (direct plus diffuse) at cloud-free times best (see uppermost panel in figure 27). The reflected shortwave radiation equals albedo times downwelling shortwave radiation (see middle panel in figure 27). The measured albedo is shown in figure 26. At low solar elevation angles the albedo reaches unity, during the day it decreases to 0.72 in the afternoon and then increases again. A possible explanation for this course could be, that on May 6th fresh snow fell and thawed, then froze to ice, explaining the high albedo during the night. During the day a small layer on the surface melts and forms a thin water film, which reduces the albedo.
The net shortwave radiation is depicted in the lowermost panel in figure 27. On the one hand, the deviation of the net radiation with constant albedo from the measured net radiation is substantial. Thus, surface albedo is a crucial factor. On the other hand, the net radiation with measured albedo is too low at times with cloud presence. The modeled cloudy sky net shortwave radiation shows a matching course to the measured one, but is generally too low. It lacks the downwelling diffuse radiation component which is not included in the simple model by Shupe and Intrieri (2004). The resulting shortwave CRF is on average -9 W/m^2 (see dark blue line in top panel of figure 29b). It is much smaller than the estimated CRF from the measurement comparison method (figure 29a). A doubling of the measured COD by the photometer gives the cyan line in figure 29b, which has a mean of -16 W/m^2. Double COD is the maximum effect of the correction proposed by Min (2004), which corrects the underestimation of the COD caused by enhanced forward scattering by cirrus clouds. Both values derived from the model are within the estimated uncertainty of -15 W/m^2 from the measurement comparison method.
Shupe and Intrieri (2004) assume that upwelling longwave radiation is not influenced by the cloud since they consider only instantaneous effects. There-

fore only the downwelling longwave radiation is modeled here. The formulae by Shupe and Intrieri (2004) lack a scaling factor for the atmospheric emission ϵ, i.e. Shupe and Intrieri (2004) assume that the atmosphere emits as a black body, opposed to other authors e.g. Dupont and Haeffelin (2008), Kruk et al. (2009). Calculating downwelling longwave radiation with the formula by Shupe and Intrieri (2004) yields too high values. Therefore, atmospheric emission terms above the cloud ϵ_{ac} and below the cloud ϵ_{bc} are introduced:

$$LW_{down}(CF=0) = t_{bc}\epsilon_{ac}\sigma T_{ac}^4 + \epsilon_{bc}\sigma T_{bc}^4, \quad (53)$$

$$LW_{down}(CF=1) = t_{bc}\epsilon_{ac}(1-\epsilon_c)\sigma T_{ac}^4 + t_{bc}\epsilon_c\sigma T_c^4 + \epsilon_{bc}\sigma T_{bc}^4, \quad (54)$$

$$CRF_{LW} = t_{bc}\epsilon_c\sigma(T_c^4 - \epsilon_{ac}T_{ac}^4). \quad (55)$$

The temperatures are calculated from the noon radiosonde profile as effective temperatures with CT denoting cloud top height, TP denoting tropopause height:

$$T_{ac} = \frac{\int_{CT}^{TP} T(z)\,\rho(z)\mathrm{d}z}{\int_{CT}^{TP} \rho(z)\mathrm{d}z}, \quad (56)$$

$$T_{bc} = \frac{\int_{0}^{CBH} T(z)\,\rho(z)\mathrm{d}z}{\int_{0}^{CBH} \rho(z)\mathrm{d}z}, \quad (57)$$

$$T_c = T(CBH). \quad (58)$$

ρ denotes the density, which is calculated from temperature, pressure and relative humidity. With an estimated CBH at 5.5 km and tropopause at 9.0 km the effective temperatures are $T_{ac} = 224\,\mathrm{K}$ (-49° C), $T_c = 243\,\mathrm{K}$ (-31° C) and $T_{bc} = 257\,\mathrm{K}$ (-16° C). The overall effective temperature is $T_{eff} = 250\,\mathrm{K}$ (-23° C). For simplicity ϵ_{ac} was set equal to ϵ_{bc}. Given that $t_{bc} = 1 - \epsilon_{bc}$ and $\epsilon_c = 1 - exp(-COD)$, ϵ_{bc} is the only free parameter. Literature suggests several possible parameterizations for ϵ (c.f. a review in Kruk et al. (2009)). In this case, the best estimate to simulate a cloud-free downwelling longwave radiation similar to the measured one was used and found to be $\epsilon_{bc} = 0.74$ (see figure 28). To keep it simple, the effective temperatures are set constant for the day. The cloudy sky downwelling longwave radiation was calculated with equation 54 with various CODs from KARL and the sun-photometer as input parameters (see figure 28). Inserting the measured COD by KARL, the measured and simulated downward longwave radiation match already quite well, but the simulated values are too low. A factor of 1.7 gives the best agreement with the measured LW_{down}. The real COD might indeed be higher than the one measured by KARL because of the multiple scattering, but the influence should be negligible for clouds with COD<1 according to Chen et al. (2002). The estimated cloud temperature is already high because the cloud base was set at the lowest reasonable height. The influence of 1 K temperature change is small. The graph with sun-photometer COD does not fit well, since it is derived from influence of clouds in the pathway of the sun and downward longwave radiation is larger for clouds in the zenith. Therefore, using COD from KARL for simu-

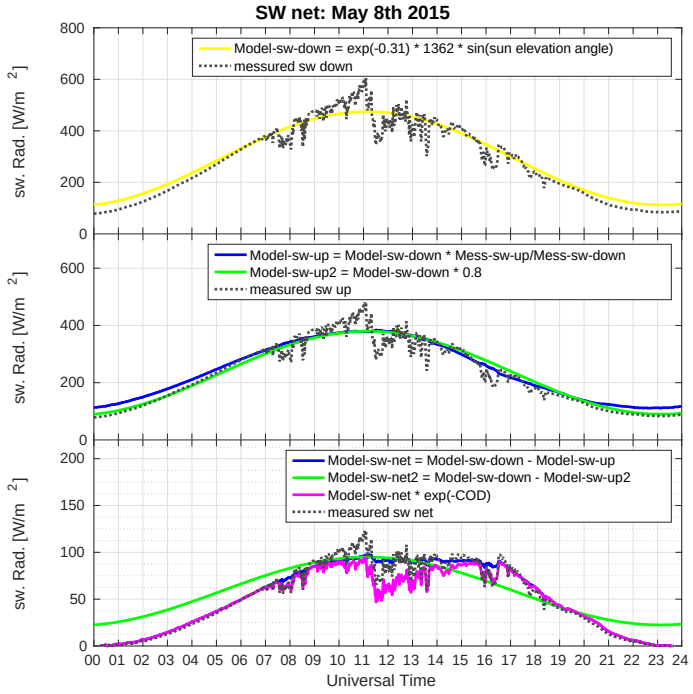

Figure 27: Depicted are the downward shortwave radiation (uppermost panel), the reflected shortwave radiation (middle panel) and the net shortwave radiation (lowermost panel) on May 8th, 2015. Dotted black lines represent the measured radiation and colored lines depict the modeled radiation. The formulae for the modeled radiation are given in the respective legends.

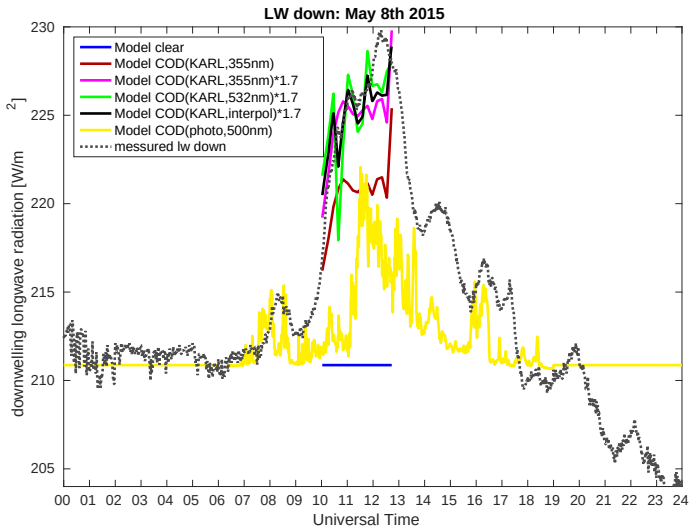

Figure 28: Depicted is the downwelling longwave radiation on May 8th, 2015. The dotted black line shows the measured downwelling longwave radiation. The blue line represents the modeled clear sky downwelling longwave radiation at times KARL was in operation. The brown, green, magenta, black and yellow lines show the modeled cloudy sky downwelling longwave radiation with different CODs: from KARL at 355 nm (brown), from KARL at 532 nm multiplied by 1.7 (green), from KARL at 355 nm multiplied by 1.7 (magenta), mean of the green and magenta line and interpolated to the minutely timescale (black), from the sun-photometer (yellow).

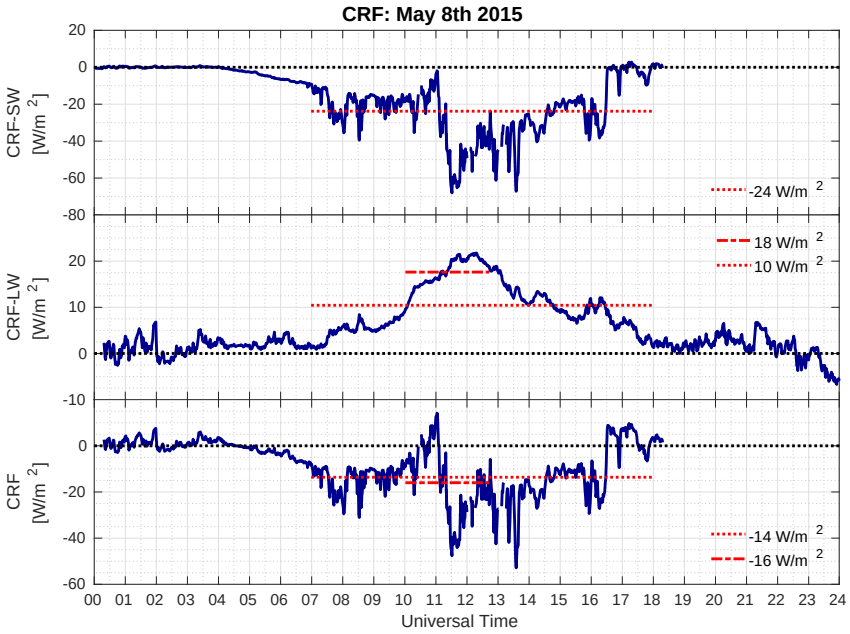

(a) Cloud radiative forcing (CRF) on May 8th, 2015 from measured radiation

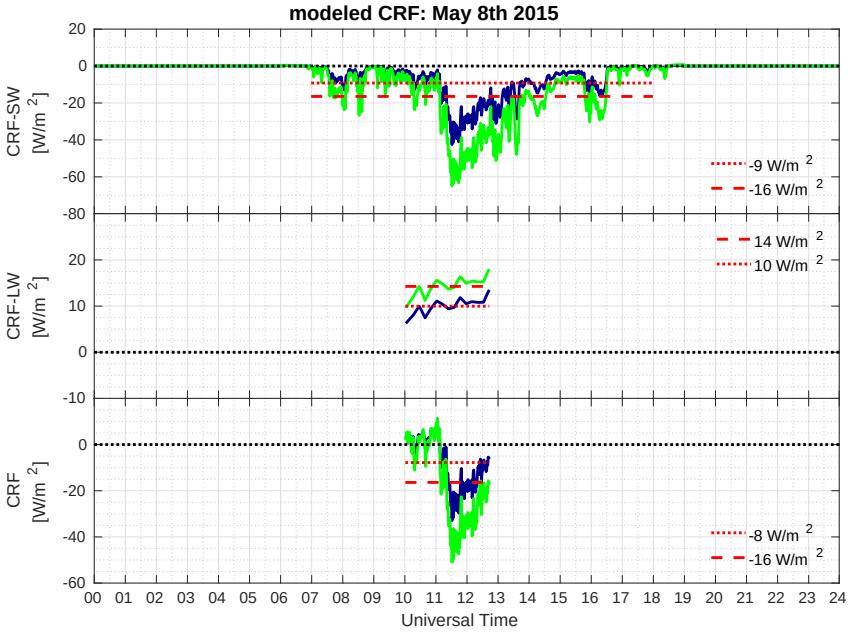

(b) Cloud radiative forcing (CRF) on May 8th, 2015 from modeled radiation with measured COD (blue) and with COD by KARL * 1.5 for the longwave and COD by sun-photometer * 2 for the shortwave CRF (green)

Figure 29: Both (a) and (b) show the shortwave cloud radiative forcing (CRF) on May 8th, 2015 in the uppermost panel, longwave CRF in the middle panel and total CRF in the lowermost panel. The red lines indicate the mean of the respective CRFs and durations. The modeled CRFs are calculated with the measured CODs (blue lines) and with double COD from the sun-photometer for shortwave and COD from KARL multiplied by 1.7 for the longwave CRF (green lines).

lating downwelling longwave radiation is the better choice. Nonetheless, the yellow graph in figure 28 indicates cloud presence and the amplitude fits roughly.
The resulting longwave CRF is depicted in the middle panel of figure 29b. The mean CRF in the time window of operation of KARL and with the interpolated measured COD is $10\,\mathrm{W/m^2}$. This is lower than the estimated $18 \pm 6\,\mathrm{W/m^2}$ from the comparison of May 8th, 2012 and 2015 within the time window 10-12:45 UT. Multiplying the COD by 1.7, which leads to the best agreement with the measured longwave fluxes, gives a mean CRF of $14\,\mathrm{W/m^2}$.
The lowermost panel of figure 29b gives the total modeled CRF. Since both shortwave and longwave CRFs are too small with opposite signs, the results of both methods only deviate by $6/\mathrm{m^2}$ with the measured COD and equalize with the enhanced input COD.

7.5 Summary

Data from the atmospheric observatory AWIPEV in Ny-Ålesund on May 8th, 2015 was used to investigate a mid day geometrically thick, high-altitude ice cloud and accompanying clouds, which impacted on the surface radiation budget for more than 10 hours. The mid day ice cloud was already optically thick enough to produce multiple scattering within the powerful Raman-lidar KARL, but still too thin to be registered by the commercial ceilometer. In addition, the ceilometer overestimated the cloud base height. Thus, despite the improvements in ceilometer technique, the CL51 from Vaisala still has a sensitivity issue detecting high ice-clouds at daylight conditions.
Two methods to derive cloud radiative forcing (CRF) were applied. Both reveal an overall negative cloud radiative forcing due to the large negative shortwave forcing and low positive longwave forcing. This is consistent with results from Dupont and Haeffelin (2008), who report a negative forcing of cirrus clouds. The comparison of BSRN measurements on May 8th, 2012 and 2015 revealed a maximum CRF of $-53\,\mathrm{W/m^2} \pm 21\,\mathrm{W/m^2}$. For a short period the cloud has a positive forcing while causing downwelling longwave and diffuse shortwave radiation without blocking the direct solar radiation. It was shown that the simple explanatory model by Shupe and Intrieri (2004) produces results close to the measurements when introducing an emissivity of the atmosphere rather than treating it as a black body and when overestimating COD. A shortcoming of the model is a lack of diffuse shortwave radiation, which is important for thin cloud radiative forcing.
Combining the sun-photometer measurements with the zenith lidar measurements is challenging due to the different measurement directions and inhomogeneities in clouds. Results from the combination of both require consideration about the general weather situation and are to be treated with caution. However, both deliver valuable information on optical properties of aerosols and thin clouds and can be utilized to estimate the radiative effects of aerosols and clouds.

8 Summary

Aim of this study has been to investigate, to what extent the measurement instruments at AWIPEV station in Ny-Ålesund, Spitsbergen, are suited for the investigation of thin clouds.

There is no generally accepted definition for thin clouds in the Arctic. Thin liquid clouds are usually distinguished by their amount of integrated liquid water per square meter (Liquid water path). The term "optically thin" refers to ice clouds or mixed-phase clouds with low liquid water content. The definition by Sassen and Cho (1992) is widely used: they call clouds with a cloud optical thickness of up to 0.3 optically thin. Between 0.3 and 10 clouds are called dense and above 10 clouds are called thick (Guerrero-Rascado et al. (2013)). Determining the amount of LWP between 0 and $40\,\mathrm{gm}^{-2}$ is crucial since this is the range where clouds have the highest warming effect on the surface (Bennartz et al. (2013)). However, measuring this low amount of LWP is still challenging. The accuracy of LWP measurements by microwave radiometry is $20\,\mathrm{gm}^{-2}$. The equivalent to this accuracy is 5 OD with droplets of effective radius r_e of 6μm and 2.5 for r_e of 12μm (Turner et al. (2007)). Hence, clouds that can be investigated with a lidar are too thin for MWR-based LWP measurements while clouds analyzable by the MWR-technique show too much multiple scattering or signal extinction in the lidar and photometer, respectively. Therefore, this study concentrates on clouds with an optical thickness below 3, to be able to use the lidar and the photometer for the characterization of the clouds' optical properties.

The mean annual course of cloudiness of the last 5 years, derived from the ceilometer, shows a general agreement with the results by Shupe et al. (2011). However, this study produces higher values of cloudiness in general and a larger transition from April to May. In addition, April is the month with the lowest interannual variability in this study while in the results of Shupe et al. (2011) it is the month with the largest variability.

It is shown in the two case studies that the sun-photometer as well as the Raman-lidar are useful tools to investigate thin clouds. The photometer has a high time resolution and is sensitive to changes in the particle size distribution and the particle number concentration of the probed atmosphere, which can inversely be concluded from the optical depth and Ångström exponent. The suggested threshold of $120\,\mathrm{W/m}^2$ direct solar radiation for the sun-photometer worked well for both case studies in separating clouds that are thick as well mountains within the field of view of the photometer from thin clouds. The advantage of the sun-photometer is that it continuously measures during polar day. But between mid October and mid March there are no measurements. Another problem is that the sun-photometer is directed at the sun whereas the lidar and the MWR are pointed in zenith direction.

The Raman lidar gives height and time resolved information on the cloud's backscatter, extinction and depolarization. From this data, conclusions on the phase and the optical thickness can be made. KARL does not measure continuously since it is expensive to operate and needs an operator. When an airplane lands or starts the lidar has to be shut-down as well. An advantage is that the

lidar is operational during polar night.
Additional temperature and humidity profiles are helpful to characterize clouds, but radiosondes are only available during mid day. Comparisons between radiosondes and MWR show that profiles from MWR are too smooth and don't show enough variability with height.
It was found that the ceilometer underestimates the presence of ice-clouds and even misses clouds with optical thickness higher than 0.3 (dense clouds). In addition, the ceilometer overestimates the cloud base height. Hence, the real occurrence of cloud cover over Ny-Ålesund is higher with lower cloud base altitudes for thin ice clouds.
The combination of measurements with different fields of view is challenging, especially for broken clouds. However, the case studies revealed that both photometer and KARL measure similar cloud optical depths. Comparisons with the course of shortwave and longwave radiation reveals, that the optical depth measured in zenith by the lidar is an indicator for the radiative effect in the longwave spectrum whilst the photometer indicates the effect on the shortwave spectrum. The backscatter-to-extinction ratio shows an unexpectedly high short-term variety. The cloud's extinction has a wavelength dependency, opposing the general assumption that clouds are grey.
The BSRN radiation data provide an excellent opportunity to derive cloud radiative forcing from measurements for both case studies. The simple model by Shupe and Intrieri (2004) can roughly explain the cloud radiative forcing measured by BSRN. However, the model needs to be tuned to the specific situation by measurements.
In a nutshell, the AWIPEV station is well equipped to investigate aerosols, optically thin clouds and their interactions.

9 Outlook

There are several open aspects in the observation of optically thin clouds and the derivation of their radiative effect on the surface, which may be addressed in future studies.
The Transregional Collaborative Research Center (TR 172) called "Arctic Amplification: Climate Relevant Atmospheric and Surface Processes, and Feedback Mechanisms", short AC^3, has been formed for "the identification, investigation, and evaluation of key processes involved in Arctic amplification; improving the understanding of the major feedback mechanisms; and quantifying the relative importance of these mechanisms" (Wendisch et al. (2017)). A coordinated campaign of the research vessel Polarstern, two airplanes and the station in Ny-Ålesund in summer 2017 will allow to i.a. investigate the latitudinal variability of water vapor, aerosols and optically thin clouds.
Suggestions for processing improvements and adjustments for future observational studies of thin clouds at Ny-Ålesund are as follows:
The literature review revealed that ice clouds produce strong forward scattering, which diminishes the apparent COD. There are several correction algorithms to derive a more accurate COD from a photometer for ice clouds by modeling and subtracting the contamination with forward-scattering. Future

work may be to apply corrections, such as suggested by Dupont and Haeffelin (2008), Guerrero-Rascado et al. (2013), Min (2004), Shiobara and Asano (1994).
The Ångström exponent of clouds may be derived more accurately in future studies by determining the AOD at each wavelength and subtracting it before determining the AE.
It would be possible to produce higher time-resolved data from KARL to study the optical properties of clouds more closely.
There are other, more sophisticated approaches to parametrize or model the clear-sky radiances (e.g. Dupont and Haeffelin (2008), Shupe and Intrieri (2004)).
Taking all these suggestions made by this study into account, one may conduct a study on optically thin Arctic clouds using a more statistical approach.

10 Acknowledgments

First, I'd like to thank Prof. Dr. Klaus Dethloff, Prof. Dr. Markus Rex and Dr. Roland Neuber for the opportunity to write my thesis in the Atmospheric Physics division at the Alfred Wegener Institute in Potsdam. It's been a pleasure to be here. My sincere thanks go to Prof. Dr. Frank Spahn for being my second referee.
Heartfelt thanks to Dr. Christoph Ritter for supporting me any time and sharing his vast experience in lidar data analysis. Many thanks to Dr. Marion Maturilli for her insights from a meteorological point of view.
Special thanks to my office mates Wenli, Paulina and Birte for sharing tea and long discussions on physics and philosophy. Thanks to my colleagues Alexander, Markus and Kati, who always had a friendly ear for problems or just a nice chat.
Huge thanks go to Birte, Christoph, Levke and Josie for proof-reading.
I am grateful to my parents, my brother and my grandparents as well as my friends for their ongoing love and support.

List of Abbreviations

Physical Quantities

AE	Ångström exponent
AOD	aerosol optical depth
CBH	cloud base height
CF	cloud fraction
CIB	cloud integrated backscatter
COD	cloud optical depth
COF	cloud occurrence fraction
CRF	cloud radiative forcing
IWV	integrated water vapor
LR	lidar ratio
LW_{down}	downwelling longwave radiation
LW_{up}	upwelling longwave radiation
LWC	liquid water content
LWP	liquid water path
SNR	signal-to-noise-ratio
SRB	net surface radiation budget
SW_{down}	downwelling shortwave radiation
SW_{up}	upwelling shortwave radiation
sza	solar zenith angle
TB	brightness temperature
TOA	top-of-the-atmosphere
VV	vertical visibility

Instruments, models and campaigns

ANN	artificial neural network
BSRN	Baseline Surface Radiation Network
KARL	Koldewey Aerosol Raman Lidar
MWR	microwave radiometer
SHEBA	Surface Heat Budget of the Arctic Ocean

List of Figures

List of References

Sun Azimuth and Elevation Calculator. Astronomical Applications Department, U.S. Naval Observatory. URL http://aa.usno.navy.mil/data/docs/AltAz.php.

A. Ansmann, U. Wandinger, M. Riebesell, C. Weitkamp, and W. Michaelis. Independent measurement of extinction and backscatter profiles in cirrus clouds by using a combined Raman elastic-backscatter lidar. *Applied Optics*, 31(33):7113, nov 1992. doi: 10.1364/ao.31.007113.

E. Bednorz, D. Kaczmarek, and P. Dudlik. Atmospheric conditions governing anomalies of the summer and winter cloudiness in Spitsbergen. *Theoretical and Applied Climatology*, 123(1-2):1–10, dec 2014. doi: 10.1007/s00704-014-1326-5.

R. Bennartz, M. D. Shupe, D. D. Turner, V. P. Walden, K. Steffen, C. J. Cox, M. S. Kulie, N. B. Miller, and C. Pettersen. July 2012 Greenland melt extent enhanced by low-level liquid clouds. *Nature*, 496(7443):83–86, apr 2013. doi: 10.1038/nature12002.

G. E. Bodeker, S. Bojinski, D. Cimini, R. J. Dirksen, M. Haeffelin, J. W. Hannigan, D. F. Hurst, T. Leblanc, F. Madonna, M. Maturilli, A. C. Mikalsen, R. Philipona, T. Reale, D. J. Seidel, D. G. H. Tan, P. W. Thorne, H. Vömel, and J. Wang. Reference Upper-Air Observations for Climate: From Concept to Reality. *Bulletin of the American Meteorological Society*, 97(1):123–135, jan 2016. doi: 10.1175/bams-d-14-00072.1.

C. F. Bohren and E. E. Clothiaux. *Fundamentals of Atmospheric Radiation*. Wiley-VCH, 2006.

C. F. Bohren, J. R. Linskens, and M. E. Churma. At What Optical Thickness Does a Cloud Completely Obscure the Sun? *Journal of the Atmospheric Sciences*, 52(8):1257–1259, apr 1995. doi: 10.1175/1520-0469(1995)052<1257:awotda>2.0.co;2.

O. Boucher. *Atmospheric Aerosols*. Springer-Verlag GmbH, 2015. ISBN 9401796483.

S. Burgemeister. Windstruktur einer arktischen Grenzschicht am Beispiel Ny-Ålesund [Wind structure of an Arctic Boundary Layer using the example of Ny-Ålesund]. Master's thesis, University of Potsdam, 12 2013.

G. Cesana, J. E. Kay, H. Chepfer, J. M. English, and G. de Boer. Ubiquitous low-level liquid-containing Arctic clouds: New observations and climate model constraints from CALIPSO-GOCCP. *Geophysical Research Letters*, 39(20):n/a–n/a, oct 2012. doi: 10.1029/2012gl053385.

T. Chen, W. B. Rossow, and Y. Zhang. Radiative effects of cloud-type variations. *Journal of Climate*, 13(1):264–286, jan 2000. doi: 10.1175/1520-0442(2000)013<0264:reoctv>2.0.co;2.

W.-N. Chen, C.-W. Chiang, and J.-B. Nee. Lidar ratio and depolarization ratio for cirrus clouds. *Applied Optics*, 41(30):6470, oct 2002. doi: 10.1364/ao.41.006470.

J. C. Chiu, C.-H. Huang, A. Marshak, I. Slutsker, D. M. Giles, B. N. Holben, Y. Knyazikhin, and W. J. Wiscombe. Cloud optical depth retrievals from the Aerosol Robotic Network (AERONET) cloud mode observations. *Journal of Geophysical Research*, 115(D14), jul 2010. doi: 10.1029/2009jd013121.

E. E. Clothiaux, T. P. Ackerman, G. G. Mace, K. P. Moran, R. T. Marchand, M. A. Miller, and B. E. Martner. Objective determination of cloud heights and radar reflectivities using a combination of active remote sensors at the ARM CART sites. *Journal of Applied Meteorology*, 39(5):645–665, may 2000. doi: 10.1175/1520-0450(2000)039<0645:odocha>2.0.co;2.

S. Crewell and U. Löhnert. Accuracy of cloud liquid water path from ground-based microwave radiometry 2. Sensor accuracy and synergy. *Radio Science*, 38(3), feb 2003. doi: 10.1029/2002rs002634.

J. A. Curry and E. E. Ebert. Annual cycle of radiation fluxes over the arctic ocean: Sensitivity to cloud optical properties. *Journal of Climate*, 5(11): 1267–1280, nov 1992. doi: 10.1175/1520-0442(1992)005<1267:acorfo>2.0.co;2.

J. A. Curry, J. L. Schramm, W. B. Rossow, and D. Randall. Overview of Arctic Cloud and Radiation Characteristics. *Journal of Climate*, 9(8):1731–1764, aug 1996. doi: 10.1175/1520-0442(1996)009<1731:ooacar>2.0.co;2.

J.-C. Dupont and M. Haeffelin. Observed instantaneous cirrus radiative effect on surface-level shortwave and longwave irradiances. *Journal of Geophysical Research*, 113(D21), nov 2008. doi: 10.1029/2008jd009838.

F. G. Fernald. Analysis of atmospheric lidar observations: some comments. *Applied Optics*, 23(5):652, mar 1984. doi: 10.1364/ao.23.000652.

C. Fröhlich and G. E. Shaw. New determination of Rayleigh scattering in the terrestrial atmosphere. *Applied Optics*, 19(11):1773, jun 1980. doi: 10.1364/ao.19.001773.

R. M. Graham, A. Rinke, L. Cohen, S. R. Hudson, V. P. Walden, M. A. Granskog, W. Dorn, M. Kayser, and M. Maturilli. A comparison of the two Arctic atmospheric winter states observed during N-ICE2015 and SHEBA. *Journal of Geophysical Research: Atmospheres*, 2016. doi: 10.1002/2016jd025475.

J. Guerrero-Rascado, M. Costa, A. Silva, and F. Olmo. Retrieval and variability analysis of optically thin cloud optical depths from a Cimel sunphotometer. *Atmospheric Research*, 127:210–220, jun 2013. doi: 10.1016/j.atmosres.2012.10.025.

A. Hoffmann. *Comparative aerosol studies based on multi-wavelength Raman LIDAR at Ny-Ålesund, Spitsbergen.* PhD thesis, University of Potsdam, 2010.

J. M. Intrieri. An annual cycle of Arctic surface cloud forcing at SHEBA. *Journal of Geophysical Research*, 107(C10), 2002. doi: 10.1029/2000jc000439.

G. H. Kaplan, J. A. Hughes, P. K. Seidelmann, C. A. Smith, and B. D. Yallop. Mean and apparent place computations in the new IAU system. III - Apparent, topocentric, and astrometric places of planets and stars. *The Astronomical Journal*, 97:1197, apr 1989. doi: 10.1086/115063.

F. Kasten. A new table and approximation formula for the relative optial air mass. *Archiv für Meteorologie, Geophysik und Bioklimatologie Serie B*, 14 (2):206–223, sep 1965. doi: 10.1007/bf02248840.

F. Kasten and A. T. Young. Revised optical air mass tables and approximation formula. *Applied Optics*, 28(22):4735, nov 1989. doi: 10.1364/ao.28.004735.

A. Kautzleben. Lidar and Dropsonde measurements during PAM-ARCMIP 2015. study project report, 09 2016.

J. D. Klett. Stable analytical inversion solution for processing lidar returns. *Applied Optics*, 20(2):211, jan 1981. doi: 10.1364/ao.20.000211.

J. D. Klett. Lidar inversion with variable backscatter/extinction ratios. *Applied Optics*, 24(11):1638, jun 1985. doi: 10.1364/ao.24.001638.

W. Komhyr. *Operations Handbook - Ozone Observations with a Dobson Spectrophotometer.* WMO Global Ozone Research and Monitoring Project, report no. 6 edition, 1980.

M. Krämer, C. Rolf, A. Luebke, A. Afchine, N. Spelten, A. Costa, J. Meyer, M. Zöger, J. Smith, R. L. Herman, B. Buchholz, V. Ebert, D. Baumgardner, S. Borrmann, M. Klingebiel, and L. Avallone. A microphysics guide to cirrus clouds – part 1: Cirrus types. *Atmospheric Chemistry and Physics*, 16(5): 3463–3483, mar 2016. doi: 10.5194/acp-16-3463-2016.

N. S. Kruk, Í. F. Vendrame, H. R. da Rocha, S. C. Chou, and O. Cabral. Downward longwave radiation estimates for clear and all-sky conditions in the Sertãozinho region of São Paulo, Brazil. *Theoretical and Applied Climatology*, 99(1-2):115–123, mar 2009. doi: 10.1007/s00704-009-0128-7.

J. Lisok, K. Markowicz, C. Ritter, P. Makuch, T. Petelski, M. Chilinski, J. Kaminski, S. Becagli, R. Traversi, R. Udisti, A. Rozwadowska, M. Jefimow, P. Markuszewski, R. Neuber, P. Pakszys, I. Stachlewska, J. Struzewska, and T. Zielinski. 2014 iAREA campaign on aerosol in Spitsbergen – Part 1: Study of physical and chemical properties. *Atmospheric Environment*, 140:150–166, sep 2016. doi: 10.1016/j.atmosenv.2016.05.051.

T. Marke, K. Ebell, U. Löhnert, and D. D. Turner. Statistical retrieval of thin liquid cloud microphysical properties using ground-based infrared and microwave observations. *Journal of Geophysical Research: Atmospheres*, 121 (24):14,558–14,573, dec 2016. doi: 10.1002/2016jd025667.

M. Maturilli and M. Kayser. Arctic warming, moisture increase and circulation changes observed in the Ny-Ålesund homogenized radiosonde record. *Theoretical and Applied Climatology*, pages 1–17, 07 2016. doi: 10.1007/s00704-016-1864-0.

M. Maturilli, A. Herber, and G. König-Langlo. Climatology and time series of surface meteorology in Ny-Ålesund, Svalbard. *Earth System Science Data*, 5:155–163, 2013. doi: 10.5194/essd-5-155-2013.

M. Maturilli, A. Herber, and G. König-Langlo. Surface radiation climatology for Ny-Ålesund, Svalbard (78.9° N), basic observations for trend detection. *Theoretical and Applied Climatology*, 120:333–339, 2015. doi: 10.1007/s00704-014-1173-4.

Q. Min. Retrievals of thin cloud optical depth from a multifilter rotating shadowband radiometer. *Journal of Geophysical Research*, 109(D2), 2004. doi: 10.1029/2003jd003964.

H. Morrison, G. de Boer, G. Feingold, J. Harrington, M. D. Shupe, and K. Sulia. Resilience of persistent Arctic mixed-phase clouds. *Nature Geoscience*, 5(1):11–17, dec 2011. doi: 10.1038/ngeo1332.

F. Pithan, B. Medeiros, and T. Mauritsen. Mixed-phase clouds cause climate model biases in Arctic wintertime temperature inversions. *Climate Dynamics*, 43(1-2):289–303, oct 2013. doi: 10.1007/s00382-013-1964-9.

R. L. Raddatz, T. N. Papakyriakou, B. G. Else, M. G. Asplin, L. M. Candlish, R. J. Galley, and D. G. Barber. Downwelling longwave radiation and atmospheric winter states in the western maritime Arctic. *International Journal of Climatology*, 35(9):2339–2351, sep 2014. doi: 10.1002/joc.4149.

HATPRO: Instrument Operation and Software Guide. Radiometer Physics GmbH, 07 2011.

HATPRO: Technical Instrument Manual. Radiometer Physics GmbH, 09 2013.

C. Ritter, R. Neuber, A. Schulz, K. M. Markowicz, I. S. Stachlewska, J. Lisok, P. Makuch, P. Pakszys, P. Markuszewski, A. Rozwadowska, T. Petelski, T. Zielinski, S. Becagli, R. Traversi, R. Udisti, and M. Gausa. 2014 iAREA camapaign on aerosol in Spitsbergern – Part 2: Optical properties from Raman-lidar and in-situ observations at Ny-Ålesund. *Atmospheric Environment*, 141:1–19, 2016. doi: 10.1016/j.atmosenv.2016.05.053.

K. Sassen and B. S. Cho. Subvisual-Thin Cirrus Lidar Dataset for Satellite Verification and Climatological Research. *Journal of Applied Meteorology*, 31 (11):1275–1285, nov 1992. doi: 10.1175/1520-0450(1992)031<1275:stcldf>2.0.co;2.

A. Schulz. Die arktische Grenzschichthöhe auf der Basis von Sondierungen am Atmosphärenobservatorium in Ny-Ålesund und im ECMWF-Modell [The Arctic Boundary Layer based on Soundings from the Atmospheric observatory in Ny-Ålesund and on the ECMWF-Model]. Master's thesis, University of Potsdam, 07 2012.

J. Sedlar, M. Tjernström, T. Mauritsen, M. D. Shupe, I. M. Brooks, P. O. G. Persson, C. E. Birch, C. Leck, A. Sirevaag, and M. Nicolaus. A transitioning Arctic surface energy budget: the impacts of solar zenith angle, surface albedo and cloud radiative forcing. *Climate Dynamics*, 37(7-8):1643–1660, nov 2010. doi: 10.1007/s00382-010-0937-5.

M. C. Serreze and R. G. Barry. Processes and impacts of Arctic amplification: A research synthesis. *Global and Planetary Change*, 77(1-2):85–96, may 2011. doi: 10.1016/j.gloplacha.2011.03.004.

M. Shiobara and S. Asano. Estimation of Cirrus Optical Thickness from Sun Photometer Measurements. *Journal of Applied Meteorology*, 33(6):672–681, jun 1994. doi: 10.1175/1520-0450(1994)033<0672:eocotf>2.0.co;2.

M. D. Shupe and J. M. Intrieri. Cloud Radiative Forcing of the Arctic Surface: The Influence of Cloud Properties, Surface Albedo, and Solar Zenith Angle. *Journal of Climate*, 17(3):616–628, feb 2004. doi: 10.1175/1520-0442(2004)017<0616:crfota>2.0.co;2.

M. D. Shupe, J. S. Daniel, G. de Boer, E. W. Eloranta, P. Kollias, E. P. Luke, C. N. Long, D. D. Turner, and J. Verlinde. A Focus On Mixed-Phase Clouds. *Bulletin of the American Meteorological Society*, 89(10):1549–1562, oct 2008. doi: 10.1175/2008bams2378.1.

M. D. Shupe, V. P. Walden, E. Eloranta, T. Uttal, J. R. Campbell, S. M. Starkweather, and M. Shiobara. Clouds at Arctic Atmospheric Observatories. Part I: Occurrence and Macrophysical Properties. *Journal of Applied Meteorology and Climatology*, 50(3):626–644, mar 2011. doi: 10.1175/2010jamc2467.1.

W. L. Smith, X. L. Ma, S. A. Ackerman, H. E. Revercomb, and R. O. Knuteson. Remote Sensing Cloud Properties from High Spectral Resolution Infrared Observations. *Journal of the Atmospheric Sciences*, 50(12):1708–1720, jun 1993. doi: 10.1175/1520-0469(1993)050<1708:rscpfh>2.0.co;2.

S. Solomon, editor. *Climate change 2007: The physical science basis: Working group I contribution to the fourth assessment report of the IPCC*. Cambridge University Press, 2007.

I. S. Stachlewska and C. Ritter. On retrieval of lidar extinction profiles using Two-Stream and Raman techniques. *Atmospheric Chemistry and Physics*, 10(6):2813–2824, mar 2010. doi: 10.5194/acp-10-2813-2010.

G. L. Stephens. *Remote Sensing of the Lower Atmosphere*. Oxford University Press, 1994.

M. Stock. *Charakterisierung der troposphärischen Aerosolvariabilität in der europäischen Arktis [Characterization of tropospheric aerosol variability in the European Arctic]*. PhD thesis, University of Potsdam and Alfred Wegener Institute, Helmholtz Centre for Polar and Marine Research, 2010.

K. Stramler, A. D. D. Genio, and W. B. Rossow. Synoptically Driven Arctic Winter States. *Journal of Climate*, 24(6):1747–1762, mar 2011. doi: 10.1175/2010jcli3817.1.

C. Tomasi, V. Vitale, A. Lupi, C. D. Carmine, M. Campanelli, A. Herber, R. Treffeisen, R. S. Stone, E. Andrews, S. Sharma, V. Radionov, W. von Hoyningen-Huene, K. Stebel, G. H. Hansen, C. L. Myhre, C. Wehrli, V. Aaltonen, H. Lihavainen, A. Virkkula, R. Hillamo, J. Ström, C. Toledano, V. E. Cachorro, P. Ortiz, A. M. de Frutos, S. Blindheim, M. Frioud, M. Gausa, T. Zielinski, T. Petelski, and T. Yamanouchi. Aerosols in polar regions: A historical overview based on optical depth and in situ observations. *Journal of Geophysical Research*, 112(D16), aug 2007. doi: 10.1029/2007jd008432.

D. D. Turner, A. M. Vogelmann, K. Johnson, M. Miller, R. T. Austin, J. C. Barnard, C. Flynn, C. Long, S. A. McFarlane, K. Cady-Pereira, S. A. Clough, J. C. Chiu, M. M. Khaiyer, J. Liljegren, B. Lin, P. Minnis, A. Marshak, S. Y. Matrosov, Q. Min, W. O. Hirok, Z. Wang, and W. Wiscombe. Thin Liquid Water Clouds: Their Importance and Our Challenge. *Bulletin of the American Meteorological Society*, 88(2):177–190, feb 2007. doi: 10.1175/bams-88-2-177.

User's Guide Vaisala Ceilometer CL51. Vaisala, 2010.

Vaisala Radiosonde RS92-SGP Datasheet. Vaisala, 2013.

M. Wendisch, M. Brückner, J. Burrows, S. Crewell, K. Dethloff, K. Ebell, C. Lüpkes, A. Macke, J. Notholt, J. Quaas, A. Rinke, and I. Tegen. Understanding Causes and Effects of Rapid Warming in the Arctic. *Eos*, jan 2017. doi: 10.1029/2017eo064803.

WMO. Guide to Meteorological Instruments and Methods of Observation. *World Meteorological Organization*, WMO-No. 8, 1996.

T. Zhang, K. Stamnes, and S. A. Bowling. Impact of Clouds on Surface Radiative Fluxes and Snowmelt in the Arctic and Subarctic. *Journal of Climate*, 9(9):2110–2123, sep 1996. doi: 10.1175/1520-0442(1996)009<2110:iocosr>2.0.co;2.

Declaration of Authorship

I hereby declare that this thesis is my own unaided work. All direct and indirect sources used are acknowledged as references.

Hiermit versichere ich, dass ich die vorliegende Masterarbeit selbstständig verfasst und keine anderen als die angegebenen Quellen und Hilfsmittel verwendet habe, wobei ich alle wörtlichen und sinngemäßen Zitate als solche gekennzeichnet habe.

Potsdam, July 26, 2017

. . . . . .

(Antje Kautzleben)